

**Shining Light on Dark Matter,  
One Photon at a Time**

by

Brandon Leigh Allen

Submitted to the Department of Physics  
in partial fulfillment of the requirements for the degree of

Doctorate of Science in Physics

at the

MASSACHUSETTS INSTITUTE OF TECHNOLOGY

June 2019

© Massachusetts Institute of Technology 2019. All rights reserved.

Author .....  
Department of Physics  
May 18, 2019

Certified by .....  
Christoph E.M. Paus  
Professor  
Thesis Supervisor

Accepted by .....  
Nergis Mavalvala  
Associate Department Head for Education



**Shining Light on Dark Matter,  
One Photon at a Time**

by

Brandon Leigh Allen

Submitted to the Department of Physics  
on May 18, 2019, in partial fulfillment of the  
requirements for the degree of  
Doctorate of Science in Physics

**Abstract**

A search is conducted for new physics in final states containing a photon and missing transverse momentum in proton-proton collisions at  $\sqrt{s} = 13$  TeV. The data collected by the CMS experiment at the CERN LHC correspond to an integrated luminosity of 35.9 inverse femtobarns. No deviations from the predictions of the standard model are observed. The results are interpreted in the context of dark matter production and limits on new physics parameters are calculated at 95% confidence level. For the two simplified dark matter production models considered, the observed (expected) lower limits on the mediator masses are both 950 (1150) GeV for 1 GeV dark matter mass.

Thesis Supervisor: Christoph E.M. Paus

Title: Professor



## Acknowledgments

This is the acknowledgements section. You should replace this with your own acknowledgements.



# Contents

<b>1 Reconstruction</b>	<b>9</b>
1.1 Tracks . . . . .	9
1.2 Primary Vertex . . . . .	9
1.3 Particle Flow . . . . .	9
1.4 Photons . . . . .	9
1.5 Electrons . . . . .	12
1.6 Muons . . . . .	12
1.7 Hadrons and jets . . . . .	12
1.8 Missing Transverse Energy . . . . .	12
1.8.1 ECAL gain-switch effect . . . . .	12
1.9 Beam Halo Phenomenology . . . . .	14
1.10 ECAL Barrel Spikes Phenomenology . . . . .	18
<b>2 Calibration</b>	<b>25</b>
2.1 Trigger Efficiency . . . . .	25
2.2 Photon Identification Efficiency . . . . .	27
2.2.1 $e/\gamma$ ID Efficiency . . . . .	28
2.2.2 $\gamma$ -specific ID Efficiency . . . . .	31
2.3 Lepton Efficiency . . . . .	41
2.4 Pileup Reweighting . . . . .	41
2.5 Lepton Veto Efficiency (Events with “Fake Leptons”) . . . . .	41
2.6 Lepton Veto Efficiency (Events with “Real Leptons”) . . . . .	42

<b>3 The Monophoton Analysis</b>	<b>45</b>
3.1 Event Selection . . . . .	46
3.2 Irreducible backgrounds . . . . .	48
3.2.1 Simulation of V+ $\gamma$ Processes . . . . .	48
3.2.2 Data-driven Control Regions . . . . .	52
3.3 Misidentified electrons . . . . .	57
3.4 Misidentified hadrons . . . . .	60
3.5 Beam halo . . . . .	63
3.6 Spikes . . . . .	65
3.7 Statistical Interpretation . . . . .	67
3.8 Results . . . . .	68
3.8.1 Pre-fit and post-fit distributions . . . . .	68
3.8.2 Limits . . . . .	71

# Chapter 1

## Reconstruction

How do we turn electrical signals into physics.

### 1.1 Tracks

### 1.2 Primary Vertex

### 1.3 Particle Flow

### 1.4 Photons

We select high- $E_T$  photons from the ECAL Barrel. First, we apply the following cuts to select high- $E_T$  photon candidates:

- Super cluster  $E_T > 175 \text{ GeV}$
- Super cluster  $|\eta| < 1.4442$ .

We use the uncorrected  $E_T$  of the supercluster as photon  $E_T$ . The use of supercluster raw  $E_T$  is motivated by an observation that this energy correction causes photon objects with large cluster shower width to exhibit unphysical energies. Figure 1-1 is a profile of the magnitude of the energy correction in bins of  $\sigma_{inj\eta}$ . As an illustration, an unphysically large correction is causing the transverse momentum of the photon

object in the event shown in Fig. 1-2 to be nearly twice as large as the  $E_T^{\text{miss}}$ , which is supposed to balance the visible, i.e., photon momentum. Photon objects with wide showers are used to estimate the hadron-to-photon misidentification background, while the photon energy resolution has an insignificant effect. Therefore, unbiased supercluster energy was chosen over the corrected photon energy.

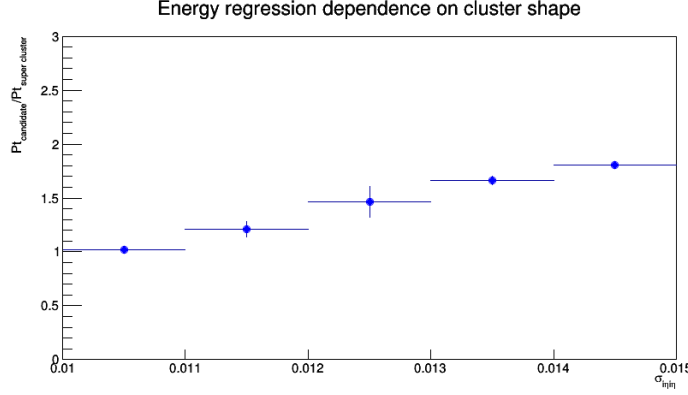


Figure 1-1: Magnitude of the energy correction on the photon object in bins of  $\sigma_{i\eta i\eta}$ .

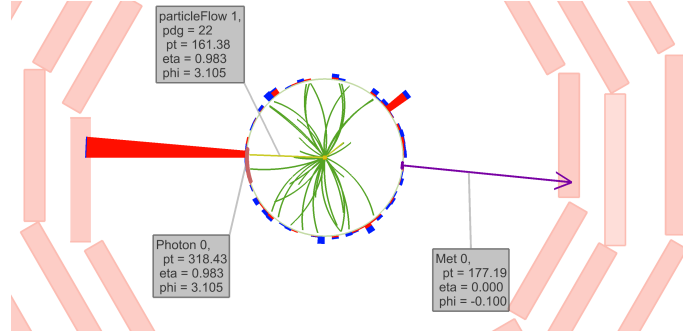


Figure 1-2: An example event where a photon with a wide shower receives a large energy correction.

To reduce hadron-to-photon misidentification rate, we apply the following collection of isolation and shower shape cuts, which will hereby be referred to as the  $e/\gamma$  ID:

- $H/E < 0.0260$
- $\sigma_{i\eta i\eta} < 0.01040$

- $\rho$ -corrected maximum PF charged hadron isolation  $I_{\text{CH}}^{\max} < 1.146 \text{ GeV}$
- $\rho$ -corrected PF neutral hadron isolation  $I_{\text{NH}} < 2.792 \text{ GeV} + 0.0112 \times E_{\text{T}}^{\gamma} + 0.000028 \times (E_{\text{T}}^{\gamma})^2 / \text{GeV}$
- $\rho$ -corrected PF photon isolation  $I_{\gamma} < 2.176 \text{ GeV} + 0.0043 \times E_{\text{T}}^{\gamma}$

In the identification criteria, the maximum PF charged hadron isolation  $I_{\text{CH}}^{\max}$  is the maximum of the standard PF charged hadron isolation computed for all reconstructed vertices. Standard PF charged hadron isolation is computed with respect to the primary vertex. Since the object with the highest  $p_{\text{T}}$  in the selected events is typically a photon, which has no intrinsic association to a vertex, it is possible that the identified primary vertex does not correspond to the  $pp$  interaction from which the photon object originate. In such cases, the photon object can be surrounded by charged hadrons, i.e., a part of a jet, and still appear isolated under the standard charged hadron isolation. The use of maximum isolation is a conservative measure to address such misidentification.

Effective areas for isolations are also recomputed to maintain flat pileup dependence as given in Table 1.1

Table 1.1: Effective areas for isolations.

Isolation	$ \eta  < 1.0$	$1.0 <  \eta  < 1.479$
maximum PF charged hadron isolation	0.01064	0.1026
PF neutral hadron isolation	0.0597	0.0807
PF photon isolation	0.1210	0.1107

To reject electrons from the candidate sample, we require that no electron track seeds can be associated to the super cluster. This is known as the pixel seed veto.

To clean the candidate sample from photon objects originating from non-collision sources. we apply the following collection of cuts, which combined with the pixel seed veto constitutes the  $\gamma$ -specific ID:

- Beam halo tagger  $E_{\text{MIP}} < 4.9 \text{ GeV}$
- $\sigma_{i\eta i\eta} > 0.001$

- $\sigma_{i\phi i\phi} > 0.001$
- Cluster seed time  $|t_{\text{seed}}| < 3 \text{ ns}$ .

Beam halo tagger is the total energy deposited in ECAL by a hypothetical beam halo muon that passes through the photon cluster. Lower bounds for  $\sigma_{i\eta i\eta}$  and  $\sigma_{i\phi i\phi}$  as well as the requirement on the cluster seed time are employed to reject spurious photon objects arising from “ECAL spikes”, or anomalous electronic signal induced at the ECAL Barrel photodetectors by nuclear or ionizing interactions in the photocathode.

## 1.5 Electrons

## 1.6 Muons

## 1.7 Hadrons and jets

## 1.8 Missing Transverse Energy

### 1.8.1 ECAL gain-switch effect

The “multi-fit” algorithm for ECAL hit reconstruction was found to have an unexpected behavior when there is a large energy deposit onto a single ECAL crystal, such that the electronic signal converted at the frontend electronics is sourced partially from channels of the preamplifier with lower gains (6 or 1) than the default (12) channel. In the most dramatic cases, pulse misreconstruction would result in underestimation by hundreds of GeV of photon  $p_T$ . This effect is mitigated in the reprocessed data set used for this analysis by identifying ECAL clusters whose seed crystal hit had a switch of gains, and performing an alternative pulse reconstruction when possible.

The gain-switch problem affected the analyses documented in this thesis, since large underestimation of the energy of a photon in an otherwise typical  $\gamma + \text{jets}$  event

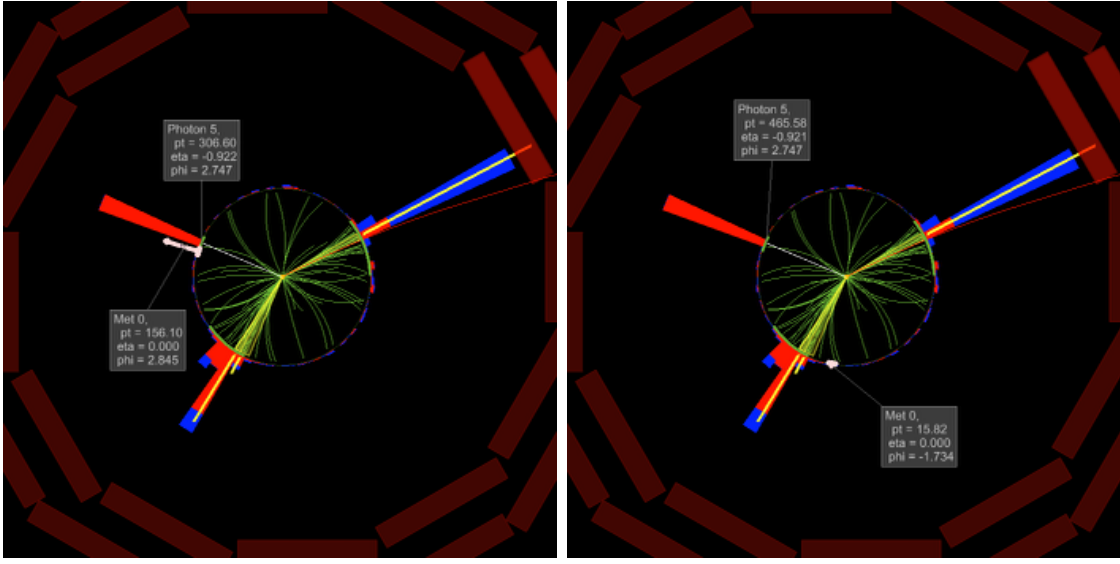


Figure 1-3: Two event displays comparing the same event, reconstructed without (left) and with (right) the fix for ECAL gain-switch effect.

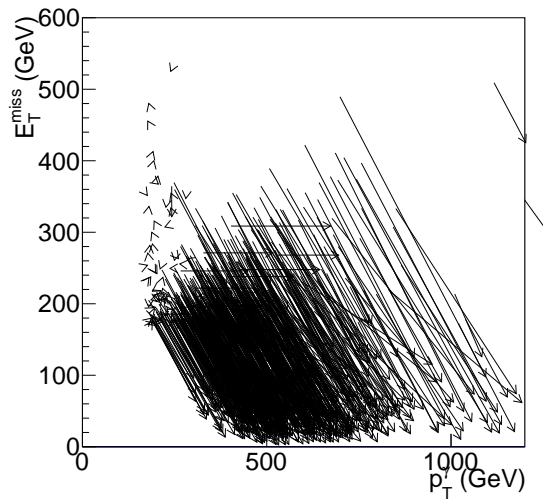


Figure 1-4: The change in reconstructed photon  $p_T$  and  $E_T^{\text{miss}}$  for events in the bin  $< 0.05$  of the distribution in Figure ???. Each arrow represents a single event, the tail (head) of the arrow corresponding to  $(E_T^{\gamma}, E_T^{\text{miss}})$  coordinates in the datasets without (with) the fix for the gain-switch problem.

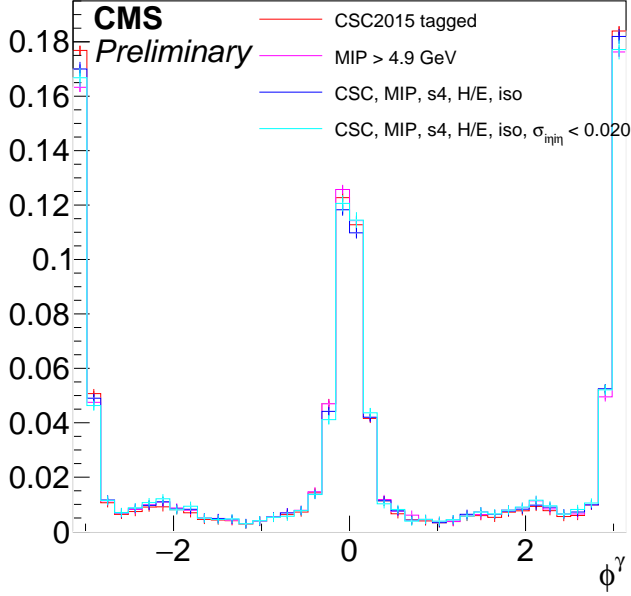


Figure 1-5: The  $\phi^\gamma$  distribution of the halo-like showers, tagged in multiple ways. Histograms are normalized to unity. The cyan histogram is the  $\phi^\gamma$  distribution after applying photon identification selections except for the shower shape. It can be seen that the  $\phi^\gamma$  distribution is highly stable against the listed identification selections.

would introduce large missing transverse momentum to the event, typical collinear to the affect photon.. Figures 1-3 and 1-4 are the visualization of how the new dataset changes the reconstructed photon energy and  $E_T^{\text{miss}}$ .

## 1.9 Beam Halo Phenomenology

Bremsstrahlung photons emitted by beam halo muons in the ECAL volume generate a physical EM shower in the ECAL crystals. Large deposits energy are rare, but the rate of beam halo penetration during the 2016 run was substantial. The characteristic features of a shower caused by a halo particle include coincident hits in the barrel muon system and a “trail” of low-energy clusters in ECAL along the particle trajectory. The beam halo MET filter described in Section 1.8 exploits the former, while the  $E_{\text{MIP}}$  variable described in Section 1.4 captures the latter.

Because beam halo particles are produced through complex LHC machine effects,

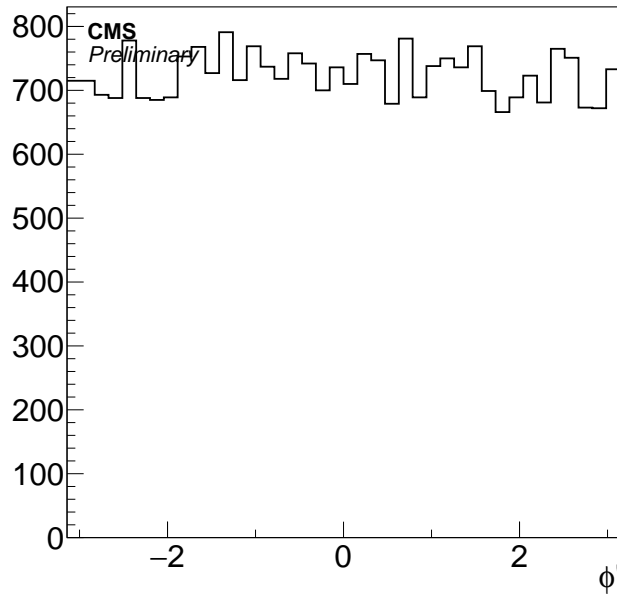


Figure 1-6: The  $\phi^\gamma$  distribution from  $Z(\rightarrow \nu\bar{\nu})+\gamma$  MC simulation.

it is natural that the observed distribution of the halo showers is not symmetric in the azimuthal angle in the detector coordinates. Figure 1-5 is a  $\phi^\gamma$  distribution of the halo showers obtained from the Single Photon data set, requiring  $E_T^{\text{miss}} > 140$  GeV. Here, halo showers are defined as those that fail the MIP-tagging and in the event tagged by the CSC beam halo tagger. On the other hand reconstructed shower from all other sources are symmetric in  $\phi^\gamma$  as demonstrated in Fig. 1-6.

For the distribution of Fig. 1-5 to be a valid template for halo showers, it must be first confirmed that its shape is invariant under photon selection requirements. However, further study of the  $\phi^\gamma$  distribution of the halo showers indicates that the relative strength of the two prominent peaks in the distribution may change under the  $\sigma_{inj}$  selection requirement. To explain this phenomenon, one needs to look at the the  $\eta^\gamma$  distribution of the shower populations near  $\phi^\gamma \sim 0$  and  $\phi^\gamma \sim \pi$ , shown in the top portion of Figure 1-7. Meanwhile, halo showers tend to have narrower shape in the  $\eta$  direction when occurring at high  $\eta$ , due to the projective geometry of the ECAL crystals, visible in the bottom portion of Figure 1-7 bottom). Combining the two observations, the conclusion is that the stringent requirement on the narrowness

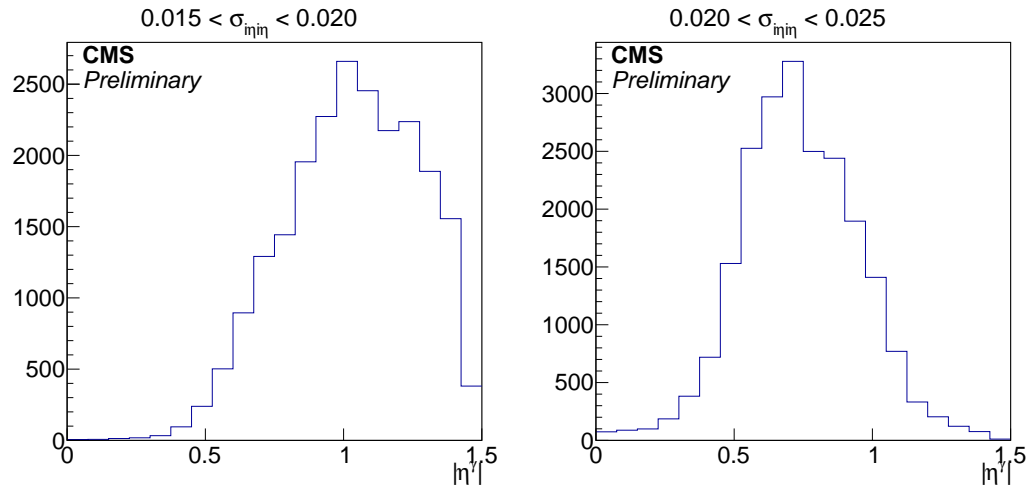
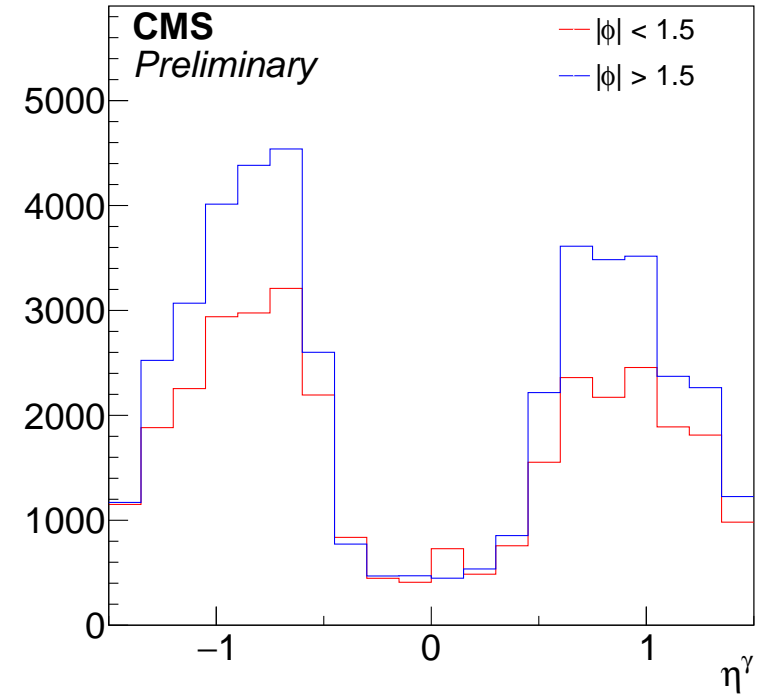


Figure 1-7: Top:  $\eta$  distribution of the halo-like showers with  $|\phi| < \pi/2$  and  $|\phi| > \pi/2$ . Bottom: shift in the  $\eta$  distribution of the halo-like showers with respect to the requirement on  $\sigma_{inj\eta}$ .

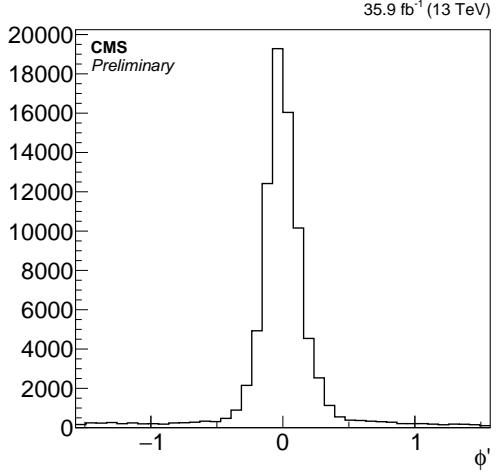


Figure 1-8: Folded  $\phi'$  distribution of the halo sample.

of the shower in the photon selection will preferentially reduce the  $\phi \sim 0$  population.

Nevertheless, the invariance under photon selection is recovered by folding the  $\phi^\gamma$  distribution such that the two peaks of the halo showers coincide. To match the positions of the peaks in the halo template, the distribution is shifted by 0.005 and then folded along 0. The new angular variable  $\phi'$

$$\phi' := \left| \left[ [\phi^\gamma + 0.005]_{-\pi}^{\pi} - \frac{\pi}{2} \right]_{-\pi}^{\pi} \right| - \frac{\pi}{2}, \quad (1.1)$$

where  $[\cdot]_\pi^\pi$  signifies casting the content into range  $[-\pi, \pi]$ , exhibits a unimodal distribution for the halo template, as shown in Fig. 1-8.

The contribution of real photons into the halo control sample is negligible. This is confirmed from the  $\sigma_{inj\eta}$  distribution of the halo control sample and the correlation between  $\sigma_{inj\eta}$  and  $E_{MIP}$  in a MC true-photon sample. The  $\sigma_{inj\eta}$  distribution of the halo control sample features a small peak at  $\sigma_{inj\eta} \sim 0.01$ , which can be attributed to contributions from true photons, as the photon  $\sigma_{inj\eta}$  distribution overlaid in Figure 1-9 suggests. However, the contribution of true photons diminishes rapidly with increasing  $\sigma_{inj\eta}$ . Additionally, Figure 1-10 illustrates that the shape of the true-photon  $\sigma_{inj\eta}$  does not change significantly with respect to  $E_{MIP}$ . From these two observations, we can see that there are only a negligible number of true photons in the halo

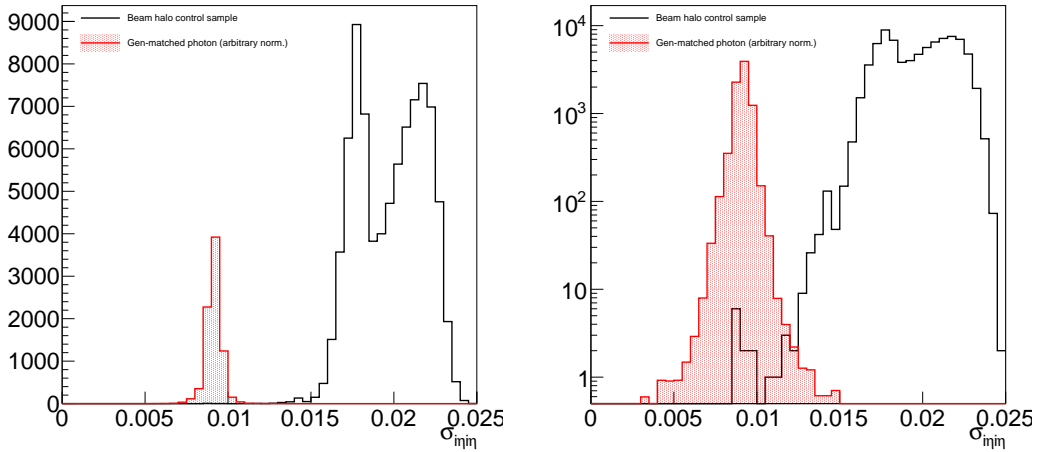


Figure 1-9: The  $\sigma_{i\eta i\eta}$  distribution of the beam halo control sample and a reference distribution from truth-matched MC photons. Left: linear scale, Right: log scale. There is a small peak at  $\sigma_{i\eta i\eta} \sim 0.01$  in the beam halo control sample, which is not visible in linear-scale.

control sample.

While the peaking behavior is a robust feature of the halo showers, their rate is not easily predictable. Therefore, the contribution from beam halo processes is estimated by a direct fit to the observed data during the signal extraction process, described in Section 3.5

## 1.10 ECAL Barrel Spikes Phenomenology

Noise in the photodetector or the detector electronics can result in spurious photon signals. Most of the time, such spurious signal is filtered out by multiple layers of protection, starting from the so-called “spike killer” algorithm at the level-1 trigger [?]. Nevertheless, in rare cases, noise in a single ECAL channel coincides with pileup or other energy deposit in the nearby crystals and appear as a high-energy photon cluster.

The origin of ECAL spikes is believed to be interactions of neutrons and other hadronic particles (collectively called neutral hadrons hereafter) with the photocathode material of the ECAL avalanche photo diodes (APD). Nuclear fission at the APD

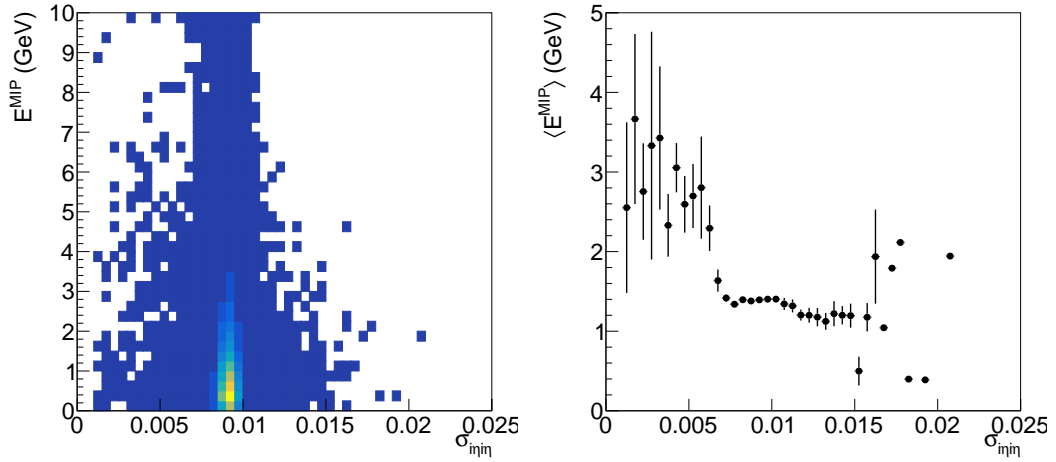


Figure 1-10: Correlation between  $\sigma_{i\eta i\eta}$  and  $E_{\text{MIP}}$  in truth-matched MC photons. Left:  $\sigma_{i\eta i\eta}$  distribution. Right: average  $E_{\text{MIP}}$  in bins of  $\sigma_{i\eta i\eta}$ .

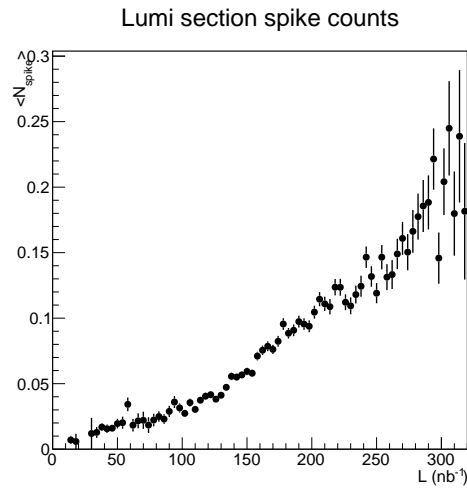


Figure 1-11: Average number of spike clusters in a luminosity section, identified by  $\sigma_{i\eta i\eta} < 0.001$  and  $E > 50 \text{ GeV}$ , in muon-triggered events, versus integrated luminosity of the luminosity section.

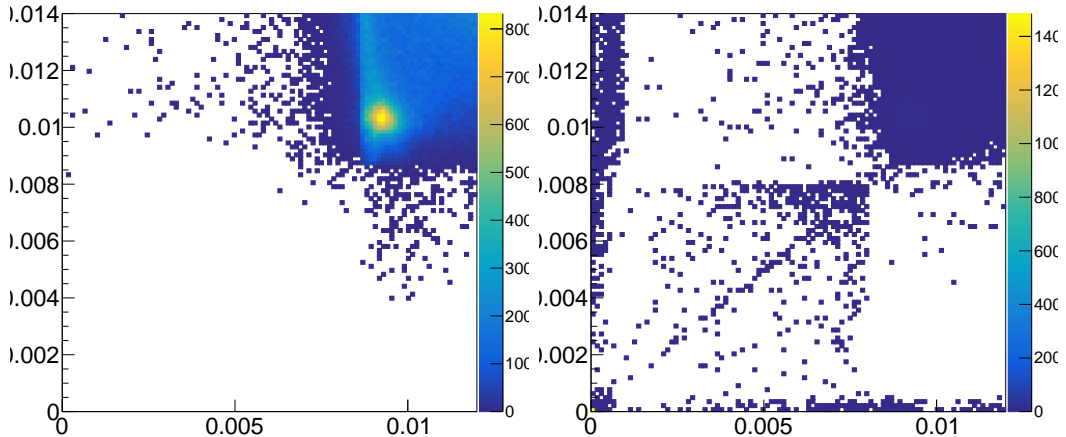


Figure 1-12: Two-dimensional distributions in  $\sigma_{i\phi i\phi}$  and  $\sigma_{inj}$  of ECAL clusters in the standard reconstruction (left) and the special reconstruction with no spike cleaning (right).

surface then causes a large electron avalanche, which is mistaken as a large photon yield scintillation in the ECAL crystal. Evidences supporting this hypothesis is documented in Ref. [?]. In Figure 1-11, scaling of the rate of spikes with the instantaneous luminosity is confirmed, up to much higher luminosity values than was observed at the time when Ref. [?] was written.

A known feature of such spurious photon clusters is that the recorded pulse shape of the seed crystal, i.e., the channel with the noise, is not what is expected from a real electromagnetic shower in ECAL. In particular, this translates to a distinctive early rec hit time distribution, since the rec hit time is extracted from a fit to the pulse shape assuming a normal pulse.

In the normal CMS data reconstruction, rec hits that are tagged as spike-like are ignored in clustering. Rec hits are tagged as spikes if there is very little energy deposit recorded in the surrounding crystals, or if the reconstructed time is out of an allowed window. Identical algorithms are employed in the HLT and offline reconstructions.

To study an unbiased spike sample, ECAL DIGI samples stored in the SingleMuon AOD datasets are reconstructed into ECAL clusters with no spike cleaning applied. DIGIs associated with the standard and “uncleaned” photon objects are stored in

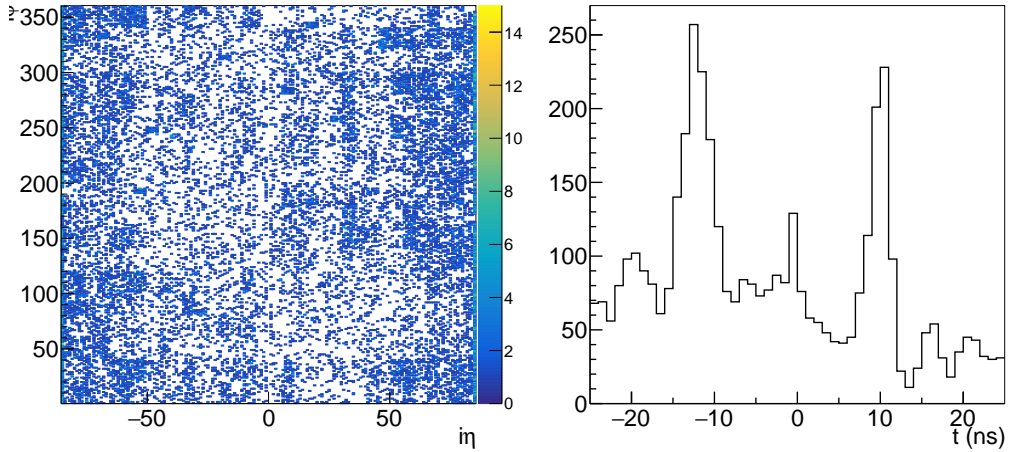


Figure 1-13:  $\eta\phi$  and time distributions of seed hits of narrow ( $\sigma_{i\eta i\eta} < 0.001$ ) clusters.

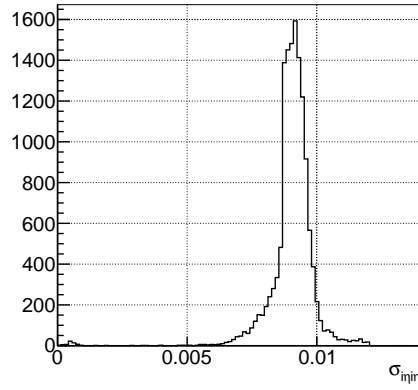


Figure 1-14:  $\sigma_{i\eta i\eta}$  distribution of uncleaned clusters from  $\gamma + \text{jets}$  MC simulation.

AOD, and ones for the uncleaned photons is rich in spike-like hits. Figure 1-12 shows how narrow clusters are cleaned away in the normal reconstruction.

Figure 1-13 shows the spacial and temporal distributions of the rec hits seeding narrow ( $\sigma_{i\eta i\eta} < 0.001$ ) clusters. The spacial distribution appears mostly random, indicating that there is no single source of spike-like rec hits. The two highest peaks in the time distribution at  $t \sim -15$  ns and  $t \sim 10$  ns are characteristic of pulse shapes, which rise faster than the pulse from the normal scintillation. The second peak is understood to come from the next bunch crossing.

The small peak at  $t \sim 0$  in the time distribution of Fig. 1-13 is due to actual

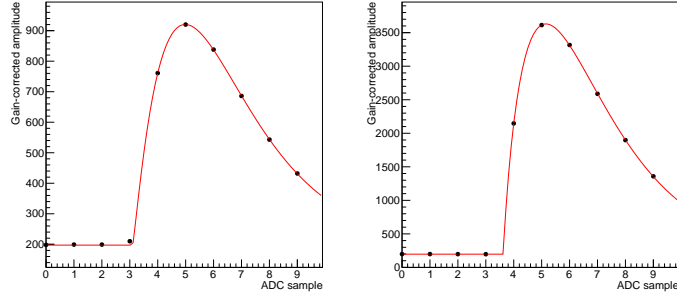


Figure 1-15: Example ECAL DIGIs and corresponding pulse shapes reconstructed through  $\chi^2$  fits of Equation 1.2, for normal (left) and spike-like (right) hits.

“physical” clusters that happened to have a very narrow cluster shape. By processing the  $\gamma$ +jets MC simulation events through this special reconstruction, we see that about 0.5% of ECAL clusters from prompt photons have  $\sigma_{i\eta i\eta} < 0.001$  as shown in Figure 1-14.

To understand the time distribution, one can investigate the original DIGI samples from which rec hits are made. At each event readout, a single ECAL channel outputs 10 ADC signals corresponding to a sampling of the analog pulse output of multi-gain preamplifier (MGPA) in range  $t_0 - 125 \text{ ns} < t < t_0 + 100 \text{ ns}$ , where  $t_0$  is the time of the triggering bunch crossing. These 10 signal points can be described well by the formula

$$f(t) = A \left(1 - \frac{t - \tau}{\alpha\beta}\right)^\alpha \exp\left(-\frac{t - \tau}{\beta}\right). \quad (1.2)$$

In the formula, parameters  $A$  and  $\tau$  correspond to the pulse amplitude and peak time, whereas  $\alpha$  and  $\beta$  control the shape of the pulse. Figure 1-15 illustrates various observed pulse shapes fit with the above formula with all parameters floating. A  $\chi^2$  fit is employed using the average noise amplitude of each MGPA channel as the errors on the data points. The noise is measured in ECAL calibration cycles in the inter-fill period and is recorded in the conditions database.

In the  $\alpha$ - $\beta$  parameter space, seed rec hits of wide clusters concentrate around  $(\alpha, \beta) \sim (1.1, 1.7)$ , while spike-like hits populate the region  $\alpha < 0.9$  as shown in

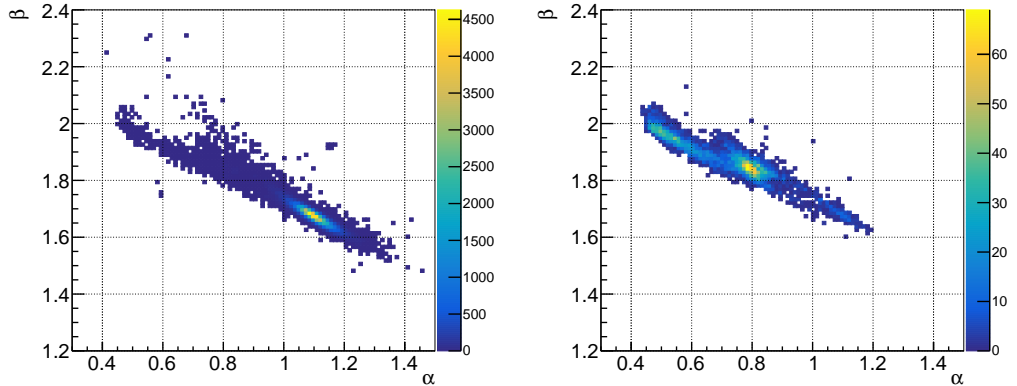


Figure 1-16:  $\alpha$ - $\beta$  distributions of the seed hits of physical wide clusters (left) and spike-like clusters (right).

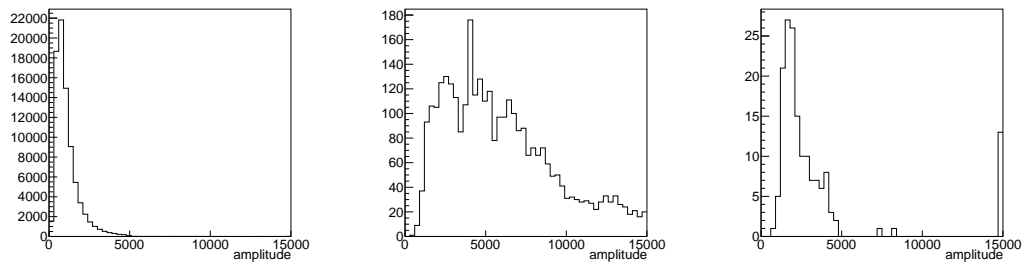


Figure 1-17: Seed crystal pulse amplitude distributions of physical wide clusters (left), narrow clusters with  $\alpha < 0.9$  (center), and narrow clusters with  $\alpha > 0.9$  (right).

Figure 1-16. In fact, the pulse amplitude distribution of narrow-cluster seeds with  $\alpha > 0.9$  is unlike that of the narrow-cluster seeds with  $\alpha < 0.9$ , and resembles the amplitude distribution of wide-cluster seeds shown in Figure 1-17. This suggests that the population  $\alpha > 0.9$  correspond to the clusters of physical, prompt photons. It then follows that spike hits can be regarded to exclusively have sharp pulse shapes.

# Chapter 2

## Calibration

Differences between data and MC efficiencies for various selections have to be corrected to achieve accurate signal and background predictions. Efficiencies of individual components are measured on data and applied to the MC.

### 2.1 Trigger Efficiency

The candidate events were recorded with the HLT\_Photon165\_HE10 trigger. The high-level trigger algorithm is relatively simple, with only a requirement of at least one  $e/\gamma$  object, reconstructed only around a L1 jet or egamma object, with  $E_T > 165 \text{ GeV}$  and  $H/E < 0.1$ , where transverse energy  $E_T$  is defined as the reconstructed energy deposit in the calorimeter cluster multiplied by the sine of the polar angle of the position of the cluster measured from the center of the detector. The variable  $H/E$  is the ratio of the energy deposit in the HCAL to that in the ECAL for a single calorimetric shower. Only the HCAL deposit in the tower behind the center of the ECAL energy deposit is considered.

Because the trigger decisions both in the L1T and HLT are based on the existence of a single object in the event, their efficiency can be measured by looking for trigger objects that match the candidate photon object in an appropriate data set. Trigger objects are the four-momenta of the objects reconstructed at the trigger level that are relevant for making trigger decisions. The match is defined by  $\Delta R = \sqrt{\Delta\eta^2 + \Delta\phi^2}$

between the two objects being less than a threshold. For the offline photon object, a line that connects the detector origin and the cluster position was used to define its direction.

The trigger efficiency measurement is performed on the SingleMuon data set, exploiting events mostly from leptonic  $t\bar{t}$  ( $e\mu$ ) topology. Events with a candidate-quality photon without electron veto requirement (see Section 1.4) and a muon object that passes the “tight” identification requirement defined in Section 1.6 and matches the trigger object of the HLT\_IsoMu24 or HLT\_IsoTkMu24 triggers are used. The matching rate of the photon object and the trigger object is the trigger efficiency. Figure 2-1 shows the L1+HLT combined efficiency as a function of the photon  $E_T$ . It can be seen that the trigger is fully efficient for  $E_T > 175$  GeV.

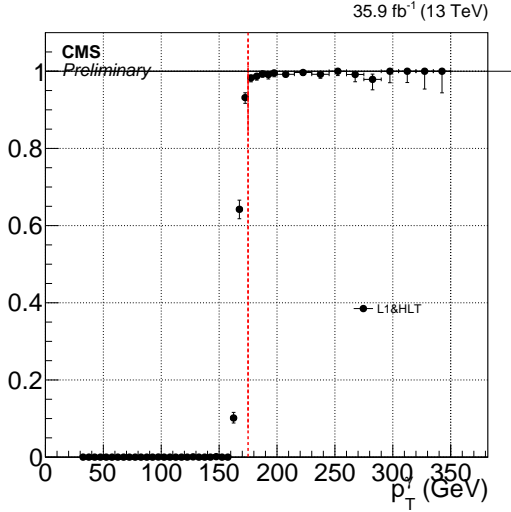


Figure 2-1: Efficiency turn-on of HLT\_Photon165\_HE10 for photons passing the candidate selection, measured using  $\mu + e/\gamma$  events from the SingleMuon data set. Red vertical line corresponds to  $E_T = 175$  GeV.

For the first period of data taking, the HLT\_Photon165\_HE10 trigger was seeded only by an isolated egamma L1 trigger. This L1 seed becomes inefficient at high  $E_T$  due to a misconfiguration in the  $H/E$  computation algorithm. The effect is visible when plotting the efficiency for a wide  $E_T$  range (Figure 2-2 left). To mitigate the effect, in the later periods, the trigger was seeded by the logical OR of SingleEG40 and SingleJet level-1 triggers. SingleJet triggers with multiple  $p_T$  threshold are combined.

Even with this addition, the measured trigger efficiency is not 100% at the plateau, but is flat with respect to  $E_T$  (Figure 2-2 right). In principle, the efficiency should be applied to all simulation-based background estimate whose normalization is fixed by theoretical calculation of the cross section. However, as discussed in Chapter 3, the dominant background in the analysis are given floating normalization that is fit to observed data, and the only simulation-based background processes with absolute normalization are those that contribute at  $\mathcal{O}(1)\%$ , with large systematic uncertainties. Therefore we deem the slight discrepancy of the trigger efficiency from unity as irrelevant.

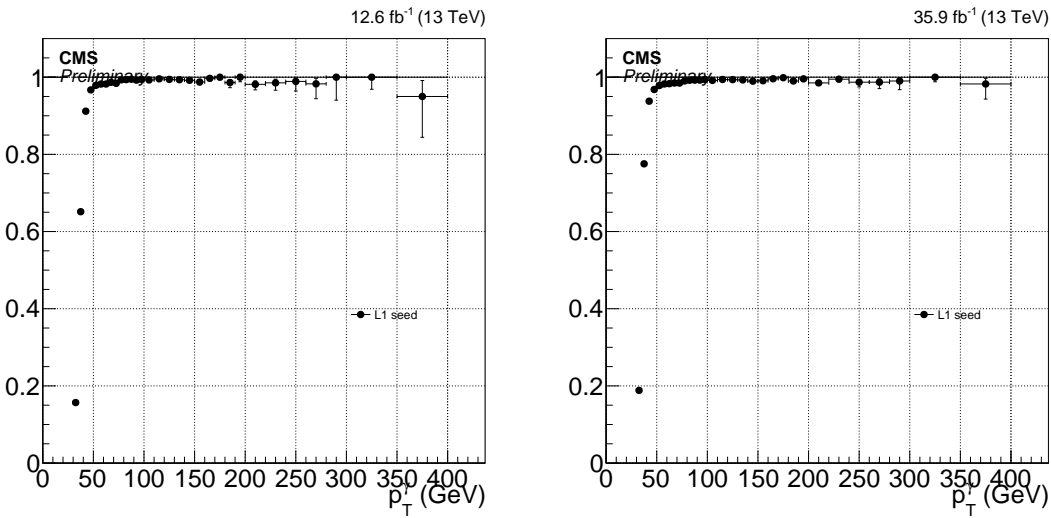


Figure 2-2: Efficiency of L1 seed for the signal trigger in periods B and C (left) and the full data set (right).

## 2.2 Photon Identification Efficiency

When measuring the photon efficiency scale factor, we split the photon ID described in Section 1.4 into two parts, which we call the  $e/\gamma$  portion and the  $\gamma$ -specific portion. The  $e/\gamma$  portion of the ID consists of the H/E,  $\sigma_{inj}$ , and PF isolation cuts and is measured using the “tag-and-probe” (TP) method as these variables have similar efficiencies for physical electrons and photons. The  $\gamma$ -specific portion of the ID consists of the pixel seed veto and non-collision rejection cuts. We measure the efficiency of

$\gamma$ -specific portion on a sample of physical photons using a  $\sigma_{i\eta i\eta}$  template fit method.

We perform both efficiency estimates as a function of  $p_T$  with the binning [175,200], [200,250], [250,300], [300,350], [350,400] and [400, $\infty$ ). This binning was chosen based on the number of available events in data for the failing probes fit in the TP method and the background template for the  $\sigma_{i\eta i\eta}$  fits.

### 2.2.1 $e/\gamma$ ID Efficiency

The efficiency corresponding to the  $e/\gamma$  part of the photon ID is estimated by exploiting the  $Z$  boson decay into an  $e^+e^-$  pair. In this “tag-and-probe” (TP) method, a high-quality electron object (tag) is identified in a single photon data sample, and the accompanying electron is sought for in the pool of electromagnetic objects (probes) in the event. The area of the peak in the mass distribution of the tag-probe system around the  $Z$  boson mass (between 81 GeV and 101 GeV) is then measured once applying the  $e\gamma$  ID requirements on the probe and once inverting the requirements. Denoting the two areas  $N_{\text{pass}}$  and  $N_{\text{fail}}$ , respectively, the resulting efficiency  $\epsilon_{e/\gamma}$  is given by

$$\epsilon_{e/\gamma} = \frac{N_{\text{pass}}}{N_{\text{pass}} + N_{\text{fail}}}. \quad (2.1)$$

The TP measurement is performed on a subset of the single photon triggered events where there is an electron object (tag) passing the “tight” identification criteria in addition to the triggering photon (probe). All possible tag-probe combinations are considered; if the tag object can also serve as a probe and the probe object as a tag, which is a common occurrence in the case when the probe is electron-like (passes the  $e\gamma$  ID), then the two combinations are considered independently to avoid the bias caused by somehow preferring one object over another to use as the probe.

The tag-probe mass distributions are then fit to extract  $N_{\text{pass}}$  and  $N_{\text{fail}}$ . The fit model is composed of two templates, where one template describes a pure  $Z \rightarrow ee$  line shape and the other describes the background contributions. The backgrounds to the fits include  $W+\text{jets}$ , diboson, and  $t\bar{t}$  productions, which are all negligible and estimated to contribute by less than 1%. Minor contribution from processes that do

not involve true electrons, such as diphoton production with a strongly asymmetric conversion on one of the photons and misidentification of a QCD jet as an electron, are predicted to be negligible from MC studies.

The  $Z \rightarrow ee$  template is given by an analytic shape of Breit-Wigner distribution convoluted with the Crystal Ball function. The mass and width parameters of Breit-Wigner distribution are fixed to PDG values. Crystal Ball parameters are allowed to float in the fit. It is well known that Breit-Wigner distribution usually does not describe the mass distribution well when the tag or the probe is under kinematically exclusive selections. However, at this high probe  $p_T$  scale, selected events are mostly of  $Z + \text{jets}$  topology with a boosted  $Z$  boson, which makes the selection rather inclusive in terms of the tag-probe invariant mass.

The background template is taken from events collected by the single photon trigger where an additional muon object is present, making use of the fact that the most of the background processes in both fits are symmetric in lepton flavor. In order to mitigate the statistical fluctuation in the background sample, the actual template is constructed by a Gaussian kernel estimation of the mass distribution of this muon-probe sample.

The floating parameters of the fits are therefore the normalizations of the  $Z \rightarrow ee$  and background templates and the Crystal Ball smearing parameters. Selected example fits are shown in Figure 2-3.

The statistical uncertainty of the fits is estimated by generating toy data from the nominal fit result with the same number of entries as the fit target distribution. The mass distribution of the toy data is then fit with the same model with the parameters floating. This procedure is repeated 100 times to obtain a distribution of the  $Z \rightarrow ee$  event yields, and its standard deviation is taken as the statistical uncertainty of the fit. Relative statistical uncertainty on the efficiency is 10%.

To estimate the effect of potential mismodeling in the fits, alternative fits varying the background and signal templates are performed first. In the alternative-background fit, a simple linear function is tested. In the alternative-signal fit, no Crystal Ball convolution is performed to the signal template and the mass and width

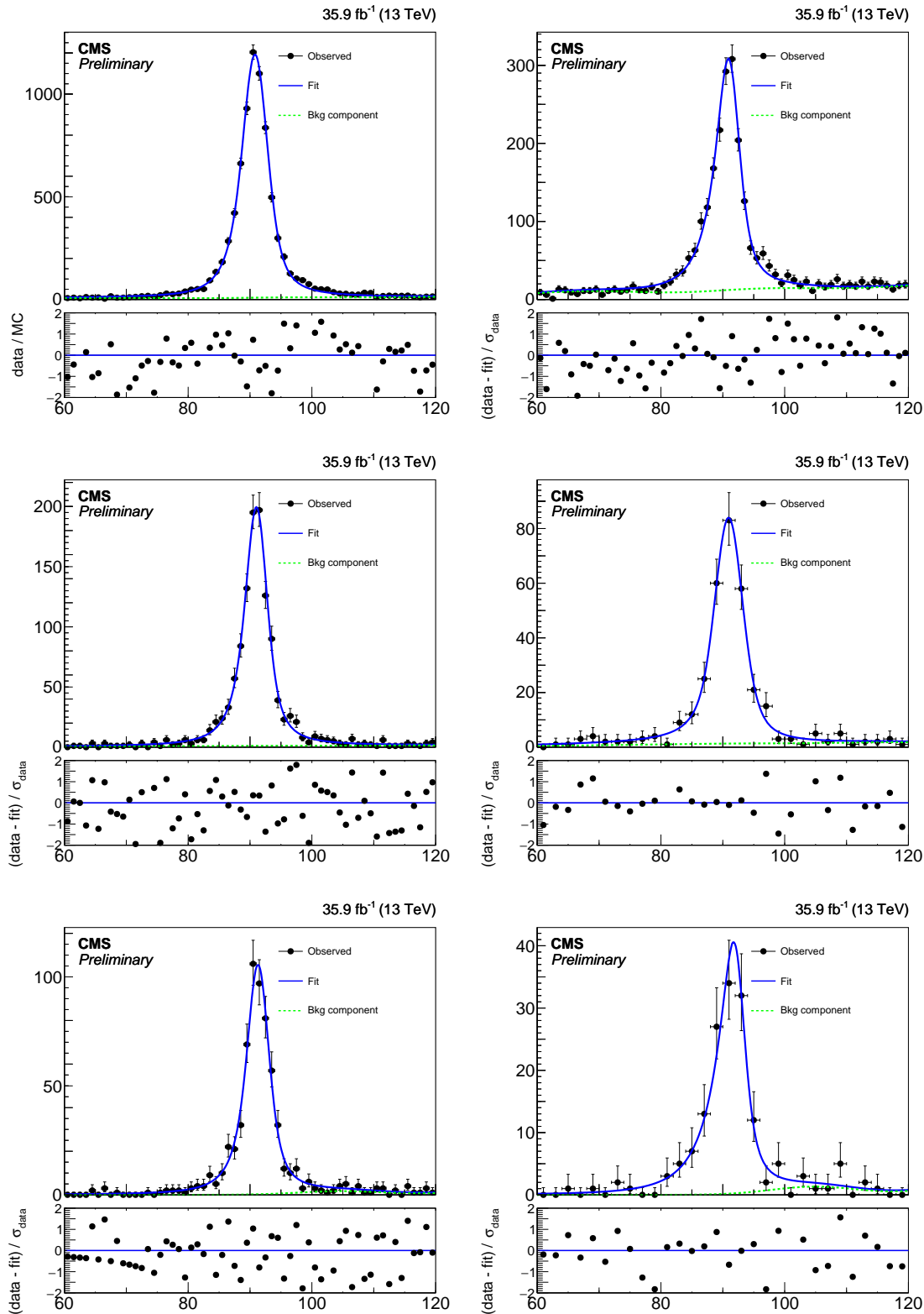


Figure 2-3: Fits to the mass distributions for pass (left) and fail (right) selections, in bins of probe  $p_T$ :  $175 < p_T < 200$  GeV (top),  $300 < p_T < 350$  GeV (middle),  $p_T > 400$  GeV (bottom). The blue solid line represents the full fit model, and the green dashed line its background component.

of the Breit-Wigner function are allowed to vary. Resulting best-fit distributions of these alternative models are then used to generate a large number of toy distributions, which are fit by the nominal model. The average shift of the fit result from the nominal value is then taken as the uncertainty. The relative uncertainty on the efficiency varies from 2 to 4% depending on the probe  $p_T$  bin.

The MC efficiency is taken from counting the number truth-matched electrons passing and failing the  $e/\gamma$  part of the ID from a  $Z \rightarrow ee$  sample. Additionally, the MC efficiency is computed using the same procedure as in data as a cross-check. The two methods are consistent within their uncertainties.

The data efficiencies, MC efficiencies, and resulting scale factors as a function of  $p_T$  are shown in Figure 2-4. The scalefactors are consistent with unity within the uncertainties. The numerical values are given in Table 2.1. We use the bin by bin scale factor corresponding to the truth values in the analysis.

Table 2.1:  $e/\gamma$  scale factors as a function of photon  $p_T$ .

$p_T^{\text{probe}}$ (GeV)	MC Fit	Truth
(175, 200)	$1.014 \pm 0.008$	$1.009 \pm 0.016$
(200, 250)	$1.003 \pm 0.008$	$0.999 \pm 0.014$
(250, 300)	$1.014 \pm 0.010$	$1.016 \pm 0.019$
(300, 350)	$1.002 \pm 0.014$	$0.997 \pm 0.022$
(350, 400)	$0.986 \pm 0.012$	$0.987 \pm 0.022$
(400, 6500)	$0.988 \pm 0.011$	$0.999 \pm 0.016$

### 2.2.2 $\gamma$ -specific ID Efficiency

To measure the efficiency of the  $\gamma$ -specific component of the photon ID, we use a  $\sigma_{i\eta i\eta}$  template fit to extract the number of true photons from a pool of photon objects passing the  $e/\gamma$  ID.

The measurement is performed over a EM object+jet control sample where we require one jet passing with  $p_T > 100$  GeV and  $|\eta| < 2.5$  which passes the loose jet ID. The EM object passes the  $e/\gamma$  ID with the exception of the following relaxed cuts:

- $\sigma_{i\eta i\eta} < 0.015$

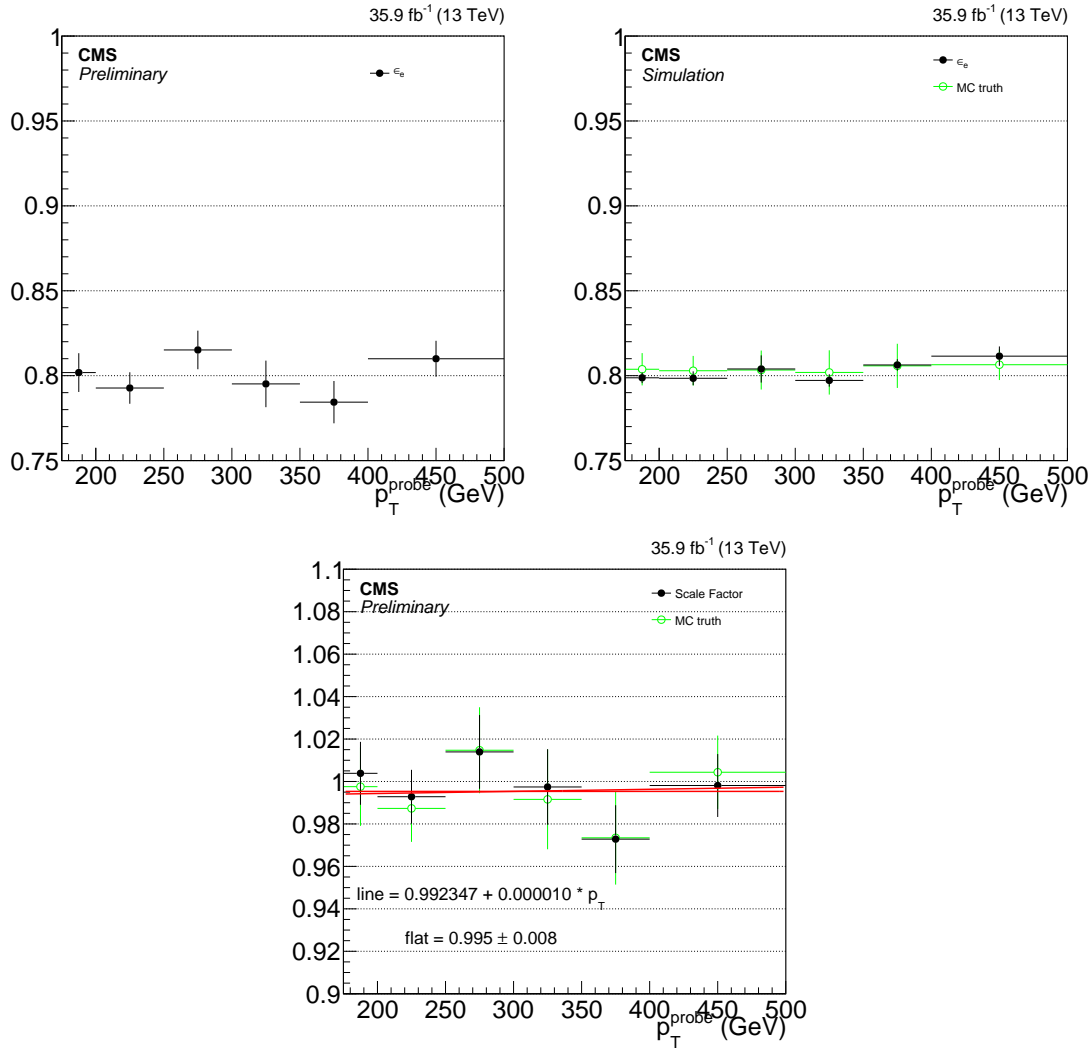


Figure 2-4:  $e/\gamma$  component of the photon identification efficiency for data (top-left) and MC (top-right) and corresponding scale factor (bottom) as a function of photon  $p_T$ .

- $I_{\text{CH}} < 11.0 \text{ GeV}$ .

Additionally, we apply a  $E_{\text{T}}^{\text{miss}} < 60 \text{ GeV}$  cut to make this region orthogonal to the signal region of the analysis.

We then fit the  $\sigma_{i\eta i\eta}$  distribution of the EM object with a template describing the  $\sigma_{i\eta i\eta}$  shape of true photons and another describing the hadronic background. The real photon template is taken from  $\gamma + \text{jets}$  MC requiring the photon to pass the  $e/\gamma$  ID except for the  $\sigma_{i\eta i\eta}$  requirement. The fake photon template is taken from the same data control sample, requiring  $5 \text{ GeV} < I_{\text{CH}} < 7 \text{ GeV}$ . The integral of the post-fit real photon template below  $\sigma_{i\eta i\eta} = 0.0104$  is the number of true photons in the target sample.

The fit is performed once for all EM objects and then once for EM objects passing the  $\gamma$ -specific ID criteria. The ratio of the numbers of true photons obtained in the two fits is the efficiency.

The  $\sigma_{i\eta i\eta}$  template fit method in its simplest form fits the observed distribution with the following fit function:

$$P(f; \sigma_{i\eta i\eta}) = f \cdot h_s(\sigma_{i\eta i\eta}) + (1 - f) \times h_b(\sigma_{i\eta i\eta}), \quad (2.2)$$

where  $h_s$  is the signal template,  $h_b$  is the background template, and  $f$  is the fraction of true photons in the target sample. Both the target template and the fit function are normalized to unity, removing the number of photon candidates in the target sample  $N$  as a fit parameter and leaving  $f$  as the only free parameter.

However, the hadronic background template, taken from the data control sample, has contributions from real photons. The amount of this “photon contamination” depends on the sideband choice, but is finite even for a sideband with very large  $I_{\text{CH}}$ . As described below, we perform additional fits with the background templates from alternative sidebands  $3.5 \text{ GeV} < I_{\text{CH}} < 5 \text{ GeV}$  (“near”) and  $7.5 \text{ GeV} < I_{\text{CH}} < 9 \text{ GeV}$  (“far”) to assess the systematic uncertainty. The photon contamination of the nominal and far sideband is 10-15%, and in the near sideband, it can go up to approximately 20% (see Figure 2-5).

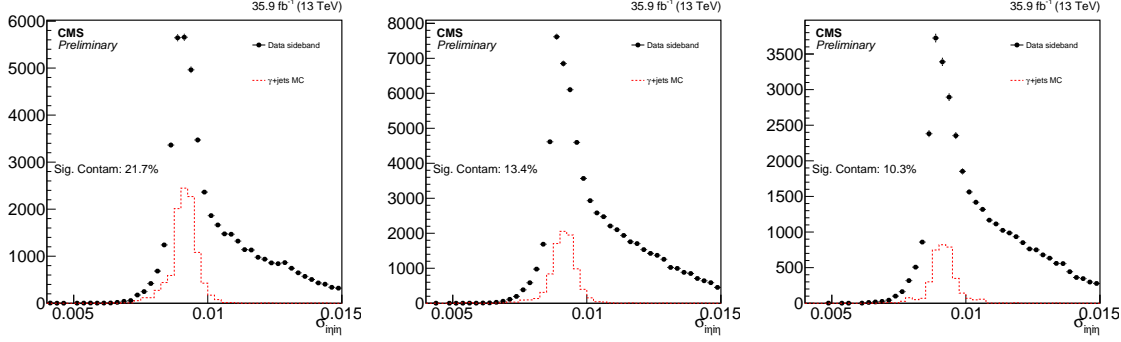


Figure 2-5: Signal contamination in the [3.5,5.0] (left), [5.0,7.5] (middle), and [7.5,9.0] (right) isolation sidebands.

To remove the photon contamination from the background templates, we modify the method and create a new background template  $h_b^{\text{sub}}$  from the original background template  $h_b$  by subtracting the true photon shape in the sideband  $h_{S'}$ . After normalization to unity, we obtain the expression

$$h_b^{\text{sub}}(\sigma_{i\eta i\eta}) = \frac{h_b(\sigma_{i\eta i\eta}) - S'/B \cdot h_{S'}(\sigma_{i\eta i\eta})}{1 - S'/B}, \quad (2.3)$$

where  $B$  is the number of photon candidates in the sideband and  $S'$  is the number of true photons in the sideband.

To determine  $S'$ , we start with the number of true photons in the target sample,  $f \cdot N$ . We then scale this by the ratio of the relative fractions of true MC photons in the  $I_{\text{CH}}$  sideband  $r_{\text{sb}}$  and in the signal region  $r_{\text{sig}}$ , giving us the expression

$$S' = f \cdot \frac{r_{\text{sb}}}{r_{\text{sig}}} \cdot N. \quad (2.4)$$

Going back to our original fit function and replacing  $h_b$  with  $h_b^{\text{sub}}$  gives us

$$P(f; \sigma_{i\eta i\eta}) = f \cdot h_s(\sigma_{i\eta i\eta}) + (1 - f) \times \frac{h_b(\sigma_{i\eta i\eta}) - S'(f)/B \cdot h_{S'}(\sigma_{i\eta i\eta})}{1 - S'(f)/B}, \quad (2.5)$$

which converges to the original fit function if  $S' = 0$ , i.e., if there is no photon contamination in the sideband. Note that  $f$  is still the only free parameter for this new function as  $S'$  only depends on  $f$  and  $r_{\text{sb}}/r_{\text{sig}}$  is set constant in the fit (see

discussion of systematics for more detail).

There are four main sources of systematic uncertainty for this measurement. The first comes from the sideband choice, as the relative rates of different types of fake photons varies with  $I_{\text{CH}}$ . The second comes from the true photon  $I_{\text{CH}}$  shape, as this is used to determine the normalization of true photons in the sideband. Currently, this shape is taken from MC and thus there is the potential to mismodel the effects of the underlying event and pile-up. The third comes from the true photon  $\sigma_{i\eta i\eta}$  distribution. As we take this from MC as well, we can mismodel the signal template shape. Finally, at high  $p_T$ , we suffer from low yields in our  $I_{\text{CH}}$  sidebands, which can lead to fluctuations that unduly influence the fit.

The uncertainty due to sideband choice is simply the larger of the differences of the purities measured using the near and far sidebands versus the nominal sideband. Figure 2-6 shows fits using the three sidebands for the  $[400, \infty)$   $p_T$  bin.

To measure the uncertainty due to the  $I_{\text{CH}}$  shape, we look at the  $I_{\text{CH}}$  for electrons in  $Z \rightarrow ee$  events in both data and MC. Using these distributions, we obtain a data/MC scale factor which we apply to the MC true photon  $I_{\text{CH}}$  distribution to obtain a scaled MC distribution. This process is shown in Figure 2-7. Then, we recount the photons using this new distribution and take the difference in the values obtained using the raw MC and scaled MC distributions as a systematic uncertainty.

To measure the uncertainty due to the signal template  $\sigma_{i\eta i\eta}$  shape, we look at the  $\sigma_{i\eta i\eta}$  distributions for electrons in both data and MC. Again we compare  $Z \rightarrow ee$  events in data and MC. From the  $\sigma_{i\eta i\eta}$  distributions of high-purity electron samples, obtain a data/MC scale factor which we apply to the MC true photon  $\sigma_{i\eta i\eta}$  distribution to obtain a scaled MC distribution. Then, we recount the photons using this new distribution and take the difference in the values obtained using the raw MC and scaled MC distributions as a systematic uncertainty. The difference between fits with and without the  $\sigma_{i\eta i\eta}$  scaling are shown in Figure 2-8.

To estimate the uncertainty due to statistical fluctuations in our background templates, we generate toys from the background template from data. We then repeat the fit with each of these toys and plot the distribution of the difference between

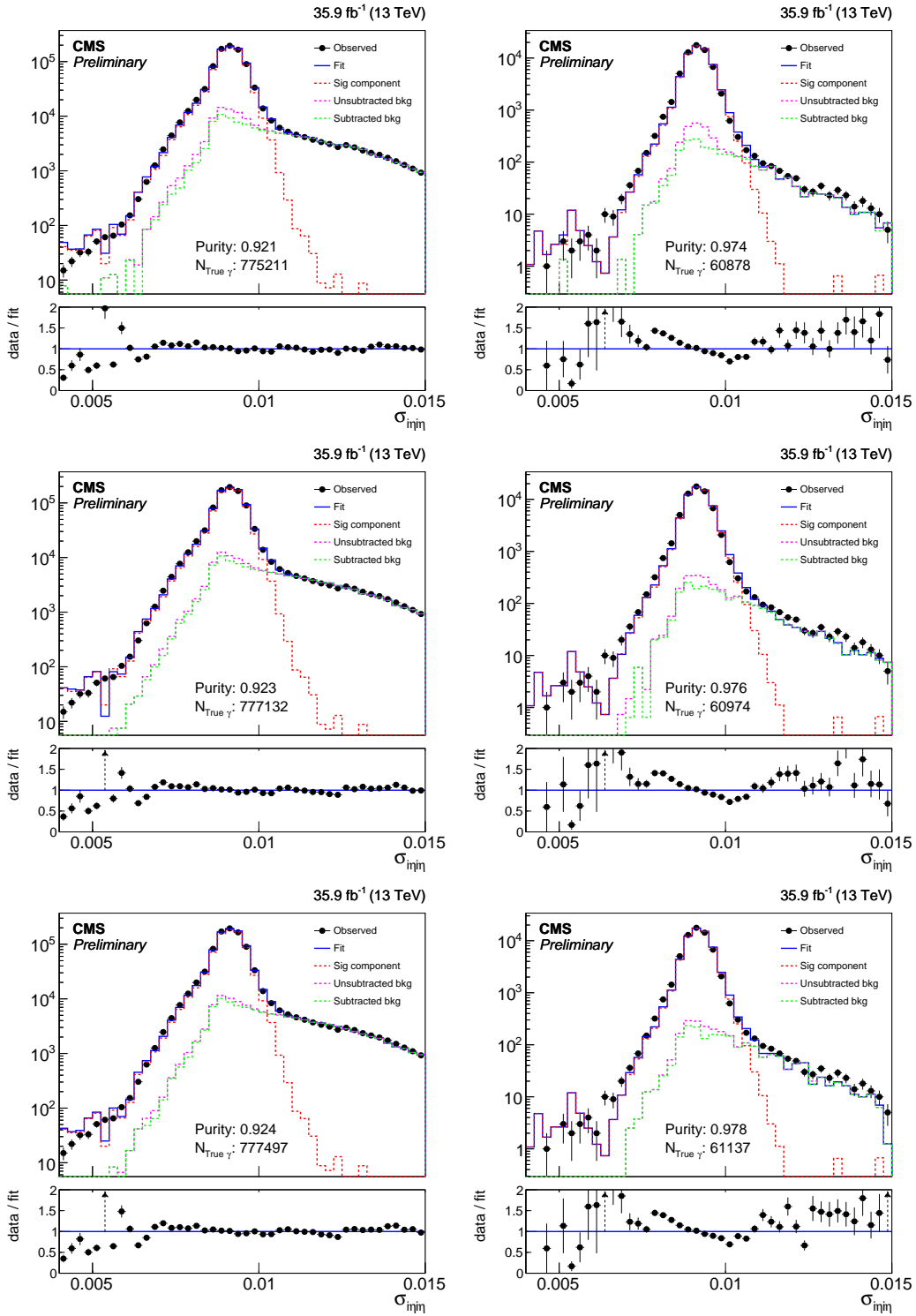


Figure 2-6: Fits to the  $\sigma_{\text{inj}\eta}$  distributions for the  $[175, 200]$  (left) and  $[400, \infty)$  (right)  $p_T$  bins using the  $[3.5, 5.0]$  (top),  $[5.0, 7.5]$  (middle), and  $[7.5, 9.0]$  (bottom) isolation sidebands. The blue solid line represents the full fit model, the red dashed line its signal component, and the green dashed line its background component.

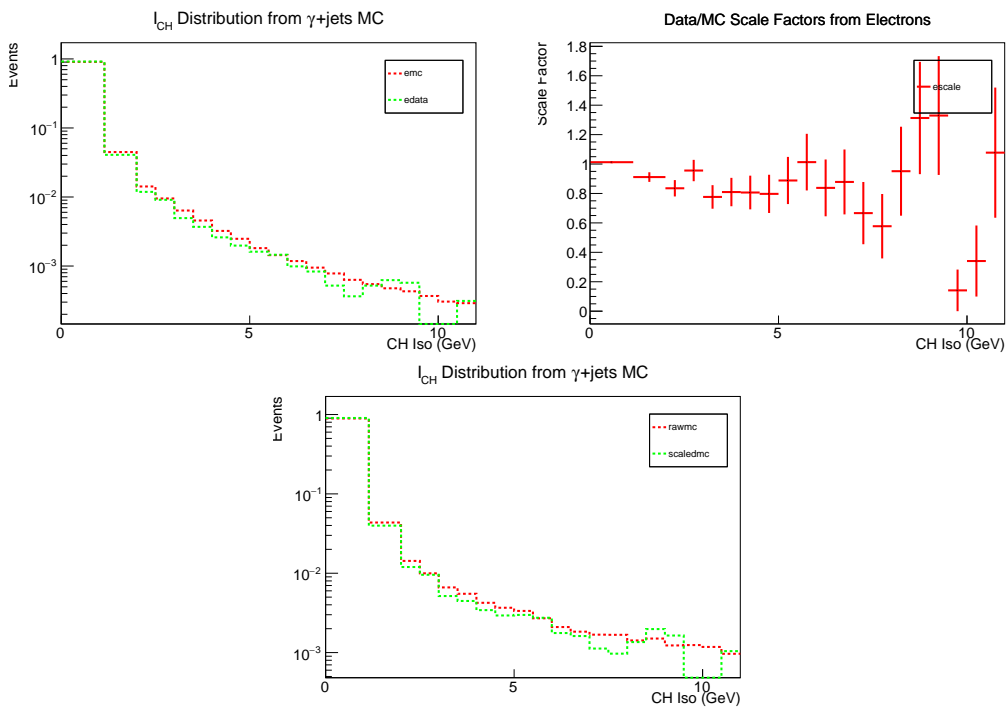


Figure 2-7: Top left:  $I_{\text{CH}}$  distributions of electrons in data and MC in  $Z \rightarrow ee$  events. Top right: data/MC scale factor obtained from the electron  $I_{\text{CH}}$  distributions. Bottom:  $I_{\text{CH}}$  distributions of the MC photon objects used to estimate the amount of photon contamination in the background template, before and after applying the data/MC scale factor.

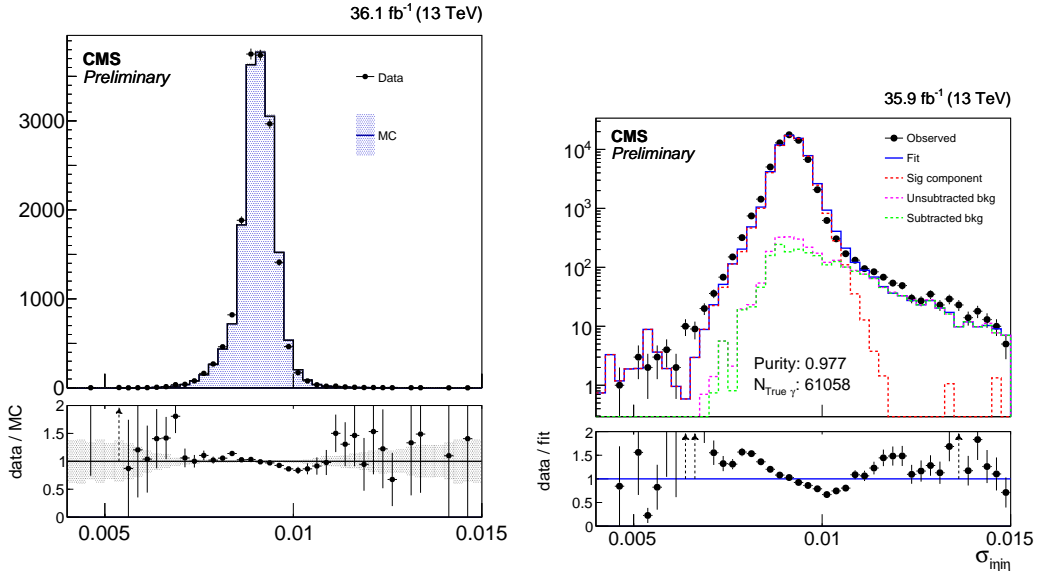


Figure 2-8: Left: Comparison of  $\sigma_{inj\eta}$  distributions between data and MC in  $Z \rightarrow ee$  events. Lower panel shows the data/MC  $\sigma_{inj\eta}$  scale factor. Right: Result of the fit with true-photon template with the data/MC  $\sigma_{inj\eta}$  scale factor applied to the true-photon template.

the purity value obtained from the toy templates versus the nominal template. We take the standard deviation of this distribution, shown in Figure 2-9, as a systematic uncertainty.

The values obtained for each systematic uncertainty on the true photon count of the denominator are shown in Table 2.2 in bins of  $p_T$ . The relative uncertainties on the numerator are similar, and in the efficiency, each uncertainty source is considered as fully correlated.

Table 2.2: Relative uncertainties on the estimated number of true photons in the denominator sample.

$p_T$ Range (GeV)	Sources of Systematic Uncertainty			
	Sideband	$I_{CH}$ Shape	Signal Shape	Bgkd. Stats
(175, 200)	0.09	0.18	0.05	0.04
(200, 250)	0.01	0.16	0.06	0.03
(250, 300)	0.14	0.16	0.06	0.05
(300, 350)	0.12	0.16	0.07	0.08
(350, 400)	0.23	0.11	0.05	0.10
(400, $\infty$ )	0.27	0.09	0.05	0.05

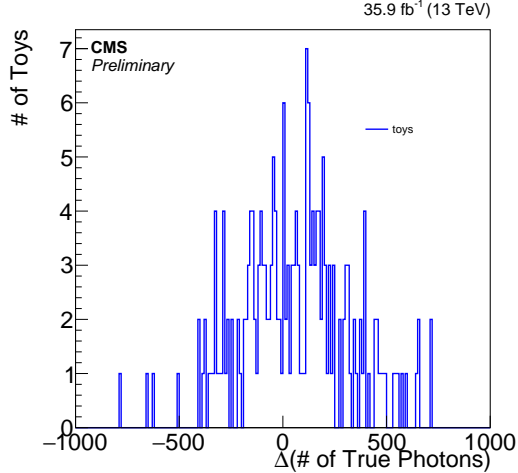


Figure 2-9: Shift in true-photon yields, extracted from alternative fits varying the background template within its statistical uncertainty. Nominal photon count in this specific  $E_T^\gamma$  bin is  $6.64 \times 10^5$ .

The MC efficiency of the  $\gamma$ -specific ID is determined by counting the number of truth-matched photons passing  $e/\gamma$  part of the ID and the full ID. However, there is a complication, the  $\gamma+jets$  region in data has approximately 5% contamination from electrons before applying the pixel veto, as shown in Figure 2-10. Thus, we combine appropriately cross-section weighted  $\gamma+jets$ ,  $W+jets$ , and  $t\bar{t}$  samples and truth match to both electrons and photons. Additionally, we apply a 14% uncertainty on the  $W+jets$  and  $t\bar{t}$  yields to account for the NLO cross-section ratio uncertainties with respect to  $\gamma+jets$  at this  $p_T$  range that is uncorrelated between the numerator and denominator as a negligible amount of electron events survive the pixel veto.

The data efficiency, MC efficiency, and the scale factor for the  $\gamma$ -specific ID as a function of  $p_T$  are shown in Figure 2-11. As there is no significant trend in the scale factor as a function of  $p_T$  we apply a flat scale factor of  $0.984 \pm 0.009$  for all of the MC-based background and signal models in the analysis.

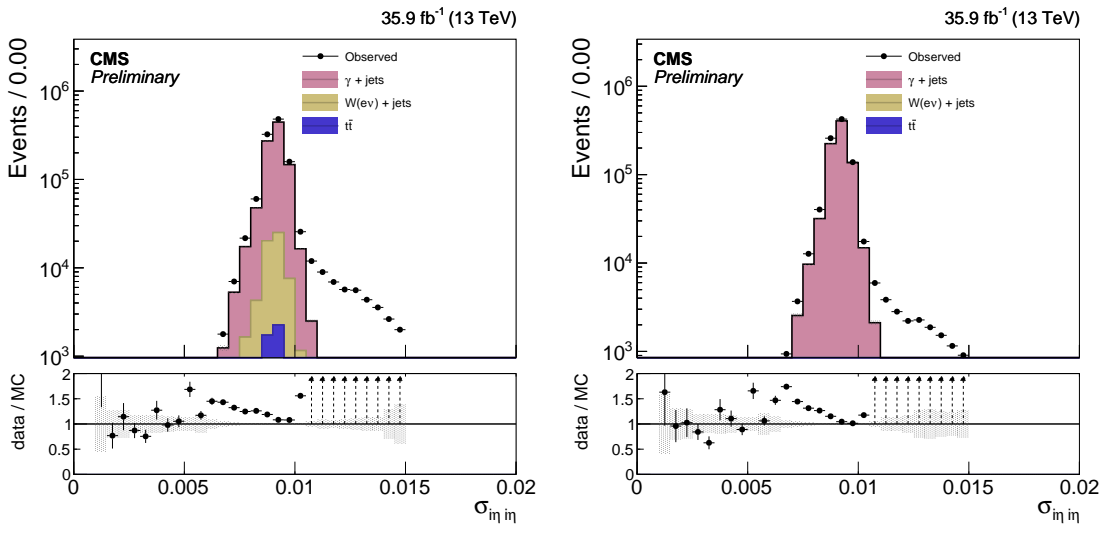


Figure 2-10: Electron contamination in  $\gamma + \text{jets}$  region before (left) and after (right) applying the pixel seed veto.

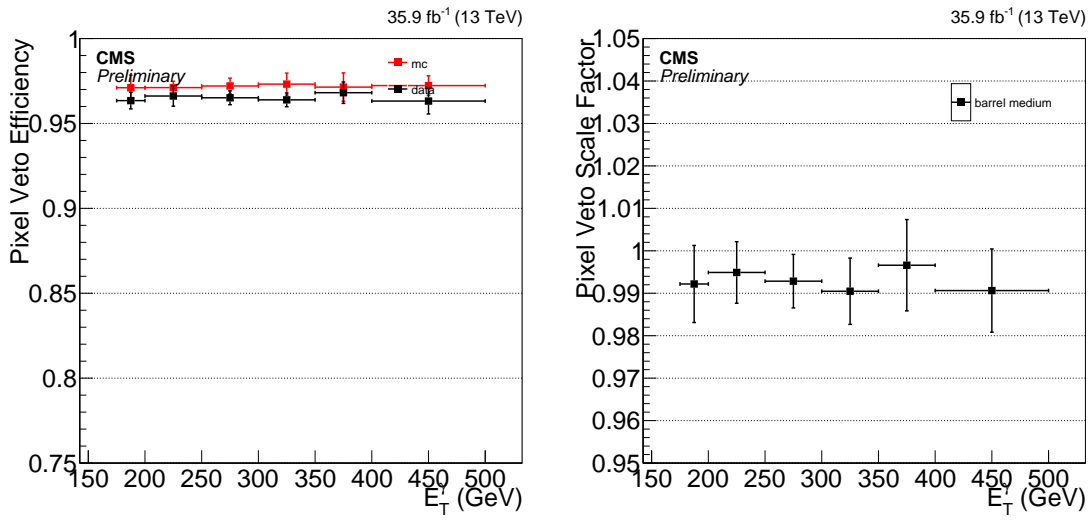


Figure 2-11: Photon pixel veto efficiencies (left) and corresponding scale factor (right) as a function of photon  $p_T$ .

## 2.3 Lepton Efficiency

## 2.4 Pileup Reweighting

The distribution of the number of pileup interactions inserted into MC events differ from the true pileup distribution, estimated from the measurement of instantaneous luminosity, beam intensity of each proton bunch, and the total cross section of proton inelastic scattering ( $69.2 \text{ mb}^{-1}$ ).

Figure 2-12 shows the pileup distributions in data and MC and their ratio. Each simulation event has its weight multiplied by the value of the ratio evaluated at the number of true pileup interaction injected into the event.

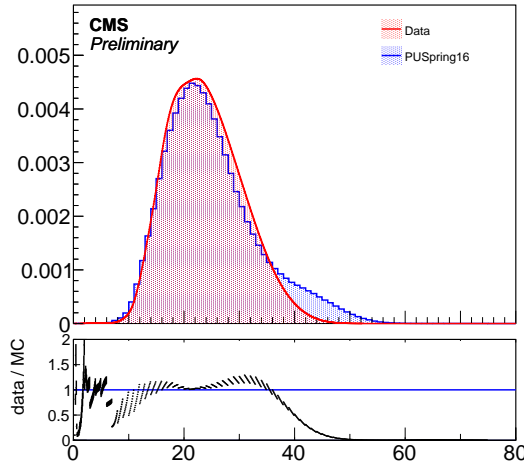


Figure 2-12: The pileup distributions in data and MC.

## 2.5 Lepton Veto Efficiency (Events with “Fake Leptons”)

The lepton veto requirement in the signal region has a non-unity efficiency over events that do not have genuine leptons, because particles such as pions and protons can mimic leptons (become “fake leptons”) and cause the event to be rejected. To measure

the possible difference between data and MC of this lepton veto efficiency, we compare dimuon events in data and MC. In a high-purity  $Z \rightarrow \mu\mu$  sample with the dimuon mass close to  $M_Z$ , events with a genuine third lepton is negligibly rare, and therefore the efficiency loss from rejecting events with a third lepton is dominantly due to fake leptons.

For this measurement, collision events are taken from the SingleMuon data set and the MC events from a mixture of DY,  $t\bar{t}$ ,  $WW$ ,  $WZ$ , and  $ZZ$  samples. We require two muons passing the “tight” identification working point defined in Section 1.6 with the mass between 61 and 121 GeV. These events are then checked for additional electron or muon objects passing the loose selection criteria defined in Sections 1.5 or 1.6, respectively. The efficiency is inspected as a function of number of vertices, number of jets, and  $H_T$  in the event, and in all cases data and MC are consistent as shown in Figure 2-13.

It should be noted, however, that the absolute lepton veto efficiency in MC dimuon sample is significantly different from that of the  $Z(\rightarrow \nu\bar{\nu})+\gamma$  sample, which more closely features the properties of the signal candidate sample. The full difference in the efficiencies between the dimuon and  $Z(\rightarrow \nu\bar{\nu})+\gamma$  samples is tentatively taken as the systematic uncertainty in the lepton veto scale factor, which is therefore  $1.00 \pm 0.02$ .

## 2.6 Lepton Veto Efficiency (Events with “Real Leptons”)

Additionally, a small fraction of events with real leptons pass the lepton veto due to the leptons failing the loose ID requirements. This effect is most relevant for  $W(\rightarrow \ell\nu)+\gamma$  events in the signal region and for  $Z(\rightarrow \ell\bar{\ell})+\gamma$  events in the single lepton control regions. We account for this effect in the following way:

Using the data and MC efficiencies from Section 2.3 for the loose IDs, we compute a scalefactor  $SF_{\text{veto}} = (1. - \epsilon_{\text{data}})/(1. - \epsilon_{\text{MC}})$  and apply this to MC events with a reconstructed lepton that fails the loose ID. If there are multiple such leptons in an

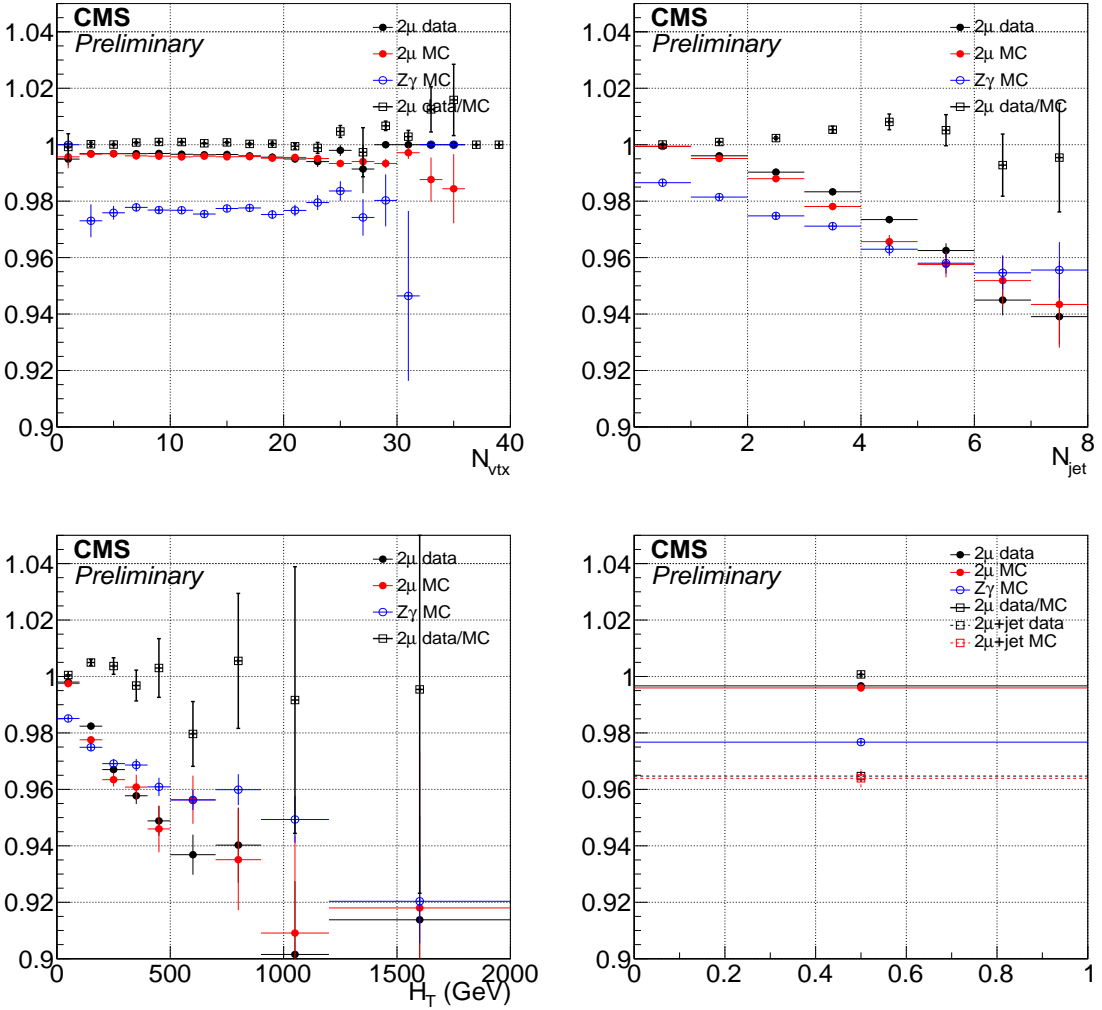


Figure 2-13: Lepton veto efficiencies and data/MC scale factors as functions of  $N_{\text{vtx}}$ ,  $N_{\text{jet}}$ , and  $H_T$ , and the corresponding inclusive values. While dimuon and  $Z(\rightarrow \nu\bar{\nu})+\gamma$  samples have significantly different efficiencies, data and MC agree well within dimuon samples, giving scale factors consistent with 1 almost everywhere. This is true even when additionally requiring a high- $p_T$  jet in the event, as seen in the inclusive efficiency plot. Thus, the difference between  $Z(\rightarrow \nu\bar{\nu})+\gamma$  and dimuon efficiencies itself is taken as the uncertainty.

event, we apply this scalefactor only for the hardest muon and electron. We apply a flat 1% (5%) uncertainty for the muon (electron) efficiencies.

The veto scale factors for electrons (muons) range from 0.55 to 1.38 (0.34 to 73.5) with uncertainties ranging from 0.15 to 1.46 (2.7 to 126.8). All scale factors are consistent with unity within the uncertainties. After applying the scale factors, the final MC yields for  $W(\rightarrow \ell\nu)+\gamma$  in the signal region and  $Z(\rightarrow \ell\bar{\ell})+\gamma$  in the single lepton control regions change by less than 0.5%.

# Chapter 3

## The Monophoton Analysis

There are multiple distinct sources of SM background to this analysis. The most significant of them are the irreducible backgrounds, which are the associated production of a high-energy  $\gamma$  with either a  $Z$  boson that subsequently decays to a pair of neutrinos or a  $W$  boson that decays to a charged lepton and a neutrino. These two processes are denoted as  $Z(\rightarrow \nu\bar{\nu})+\gamma$  and  $W(\rightarrow \ell\nu)+\gamma$ , respectively, and together they account for approximately 70% of the SM background, with 50% from the former and 20% from the latter. The total irreducible background rate is estimated using simultaneous fits to the signal and control regions defined in Section 3.1 and the details of the modeling are given in Section 3.2.

Less significant but non-negligible backgrounds arise from events where the candidate photon object is a misidentified electron (Section 3.3) or electromagnetic shower caused by hadrons (Section 3.4). The background events from electron misidentification are mostly  $W$  boson production ( $W \rightarrow e$ ), whereas those from hadron misidentification can be due to multiple sources such as  $Z(\rightarrow) + \text{jets}$  and QCD multijet with grossly mismeasured jet energy. Misidentification itself is rare, but all of the above processes have high cross sections. Since object misidentification rates depend on subtle details of the detector, the MC simulation cannot be expected to model it reliably. Therefore, data-driven techniques are employed to estimate the contributions from these background events.

After the full selection described in Section 3.1, the SM  $\gamma+\text{jets}$ ,  $t\bar{t}\gamma$ ,  $VV\gamma$ ,  $Z(\rightarrow$

$\ell\bar{\ell})+\gamma$ , and  $W \rightarrow \ell\nu$  processes are minor ( $\sim 10\%$ ) background processes in the signal region. These processes, collectively denoted as minor SM backgrounds, can contribute in the signal region if the jet energy is severely mismeasured or the leptons fail to be reconstructed resulting in large  $E_T^{\text{miss}}$  in the signal region. However, the  $E_T^{\text{miss}}$  is typically aligned with the photon or one of the jets in such cases, and therefore various selections on the kinematic relations between the  $E_T^{\text{miss}}$ , photons, and jets are used to reduce these backgrounds to a manageable rate. The estimates for all five processes are taken from MADGRAPH5\_aMC@NLO simulations at LO in QCD and can be found in Tables 3.4 and 3.5.

Finally, apparent large energy deposits in ECAL from non-collision processes can mimic  $\gamma+E_T^{\text{miss}}$  events and therefore need to be controlled. Known sources of such background include bremsstrahlung of beam halo or cosmic ray muons and anomalous ECAL energy deposits resulting from the interaction of particles in the ECAL photodetectors referred to as “ECAL spikes”. These processes are described in detail in Sections 3.5 and 1.10, respectively.

All background processes except for the two irreducible ones and beam halo are given absolute estimates from data-driven methods or MC cross section calculations. The estimates of the contributions from  $Z(\rightarrow \nu\bar{\nu})+\gamma$ ,  $W(\rightarrow \ell\nu)+\gamma$ , and beam halo processes are allowed to float in the final fit to data performed to extract the potential signal contribution described in Section 3.7.

### 3.1 Event Selection

The integrated luminosity of the analyzed data sample is  $(35.9 \pm 0.9) \text{ fb}^{-1}$  [?]. The data sample is collected with a single-photon trigger that requires at least one photon candidate with  $p_T > 165 \text{ GeV}$ . The photon candidate must have  $H/E < 0.1$  to discriminate against jets, where  $H/E$  is the ratio of HCAL to ECAL energy deposits in the central calorimeter tower corresponding to the candidate. The photon energy reconstructed at the HLT is less precise relative to that derived later in the offline reconstruction. Therefore, the thresholds in the trigger on both  $H/E$  and  $E_T^\gamma$ , are

less restrictive than their offline counterparts. The trigger efficiency is measured to be about 98% for events passing the analysis selection with  $E_T^\gamma > 175 \text{ GeV}$ .

From the recorded data, events are selected by requiring  $E_T^{\text{miss}} > 170 \text{ GeV}$  and at least one photon with  $E_T^\gamma > 175 \text{ GeV}$  in the fiducial region of the ECAL barrel ( $|\eta| < 1.44$ ) passing the selected presented in Section 1.4.

Events with a high- $p_T$  photon and large  $E_T^{\text{miss}}$  are subjected to further requirements to suppress SM background processes that feature a genuine high-energy photon, but not a significant amount of  $E_T^{\text{miss}}$ . One such SM process is  $\gamma + \text{jets}$ , where an apparent large  $E_T^{\text{miss}}$  is often the result of a mismeasured jet energy. In contrast to signal processes,  $E_T^{\text{miss}}$  is typically smaller than  $E_T^\gamma$  in these events, so requiring the ratio of  $E_T^\gamma$  to  $E_T^{\text{miss}}$  to be less than 1.4 rejects this background effectively with little effect on signal efficiency. Events are also rejected if the minimum opening angle between  $\vec{p}_T^{\text{miss}}$  and the directions of the four highest  $p_T$  jets,  $\min\Delta\phi(\vec{p}_T^{\text{miss}}, \vec{p}_T^{\text{jet}})$ , is less than 0.5. Only jets with  $p_T > 30 \text{ GeV}$  and  $|\eta| < 5$  are considered in the  $\min\Delta\phi(\vec{p}_T^{\text{miss}}, \vec{p}_T^{\text{jet}})$  calculation. In the  $\gamma + \text{jets}$  process, rare pathological mismeasurement of  $E_T^\gamma$  can also lead to large  $E_T^{\text{miss}}$ . For this reason, the candidate photon  $\vec{p}_T$  and  $\vec{p}_T^{\text{miss}}$  must be separated by more than 0.5 radians. Another SM process to be rejected is  $W(\rightarrow \ell\nu) + \gamma$ , for which events are vetoed if they contain an electron or a muon with  $p_T > 10 \text{ GeV}$  that is separated from the photon by  $\Delta R > 0.5$ . Furthermore, using features described in Section 3.5, the signal region is split into two parts according to  $\phi$  to constrain the beam halo normalization. The region defined by  $|\sin(\phi)| < \sin(0.5)$  is called the horizontal region, and its complement in  $\phi$  is called the vertical region.

The residual contributions from the  $W(\rightarrow \ell\nu) + \gamma$  process, where the lepton could not be identified or was out of the detector acceptance, are modeled by fitting to observed data, as described in Section 3.2. The same method is employed to model the contribution from the  $Z(\rightarrow \nu\bar{\nu}) + \gamma$  process to the signal region. This method utilizes control regions where one or two leptons (electrons or muons) are identified in addition to the photon, as defined in the following.

The single-electron (single-muon) control region is defined by a requirement of exactly one electron (muon) with  $p_T > 30 \text{ GeV}$  and  $|\eta| < 2.5$  (2.4) in addition to a

photon requirement that is identical to the one for the signal region. To suppress the contributions from large- $E_{\mathrm{T}}^{\text{miss}}$  processes other than  $W(\rightarrow \ell\nu)+\gamma$ , the transverse mass  $m_{\mathrm{T}} = \sqrt{2E_{\mathrm{T}}^{\text{miss}} p_{\mathrm{T}}^{\ell} [1 - \cos \Delta\phi(\vec{p}_{\mathrm{T}}^{\text{miss}}, \vec{p}_{\mathrm{T}}^{\ell})]}$  must be less than 160 GeV. Additionally, for the single-electron control region,  $E_{\mathrm{T}}^{\text{miss}}$  must be greater than 50 GeV to limit the contribution from the  $\gamma+\text{jets}$  process, where a jet is misidentified as an electron. Finally, the recoil vector  $\vec{U} = \vec{p}_{\mathrm{T}}^{\text{miss}} + \sum \vec{p}_{\mathrm{T}}^{\ell}$ , which serves as this region's analogue for  $\vec{p}_{\mathrm{T}}^{\text{miss}}$  in the signal region, must satisfy identical requirements to those for the  $\vec{p}_{\mathrm{T}}^{\text{miss}}$  in the signal region.

The dielectron (dimuon) control region is defined by exactly two electrons (muons) in addition to the photon, with  $60 < m_{\ell\ell} < 120$  GeV, where  $m_{\ell\ell}$  is the invariant mass of the dilepton system. The recoil vector of this region is  $\vec{U} = \vec{p}_{\mathrm{T}}^{\text{miss}} + \sum \vec{p}_{\mathrm{T}}^{\ell}$  and must satisfy identical requirements to those for the  $\vec{p}_{\mathrm{T}}^{\text{miss}}$  in the signal region.

## 3.2 Irreducible backgrounds

### 3.2.1 Simulation of $V+\gamma$ Processes

The  $Z(\rightarrow \nu\bar{\nu})+\gamma$  and  $W(\rightarrow \ell\nu)+\gamma$  background contributions are modeled using MC simulations. Samples generated at the leading order (LO) in QCD by MADGRAPH 5 with up to two additional partons and a generator-level requirement of  $E_{\mathrm{T}}^{\gamma} > 130$  GeV are employed for this purpose.

A study using a privately generated aMC@NLO sample with high  $E_{\mathrm{T}}^{\gamma}$  threshold confirms that the predicted kinematic distributions would not change drastically by using the NLO sample. Figures 3-1 and 3-2 show the comparisons of the private aMC@NLO samples and the MADGRAPH 5 samples used for the background estimation in the key kinematic distributions.

To approximate the QCD higher-order effects,  $Z(\rightarrow \nu\bar{\nu})+\gamma$  and  $W(\rightarrow \ell\nu)+\gamma$  events are reweighted with  $E_{\mathrm{T}}^{\gamma}$  by the factors given in Tab. 3.1. These factors are the ratios of QCD next-to-next-to leading order (NNLO) differential cross sections calculated by Grazzini et al. [?] to the LO cross sections given in the centrally pro-

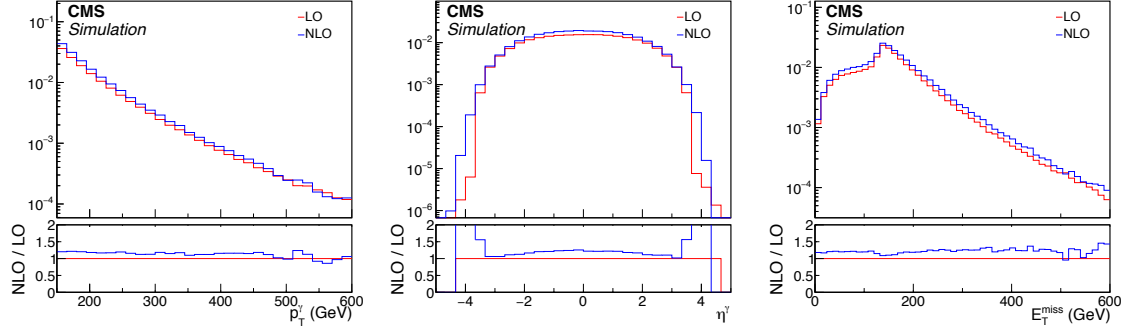


Figure 3-1: Distributions of  $E_T^\gamma$  (left),  $\eta^\gamma$  (middle), and  $p_T^Z$  (right) in  $Z(\rightarrow \nu\bar{\nu}) + \gamma$  process from the private aMC@NLO sample (blue) and the LO sample used for background prediction (red) along with the NLO / LO ratios.

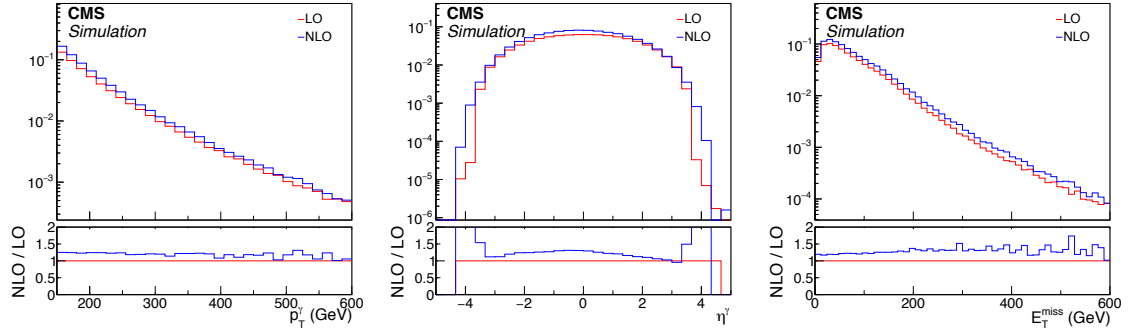


Figure 3-2: Distributions of  $E_T^\gamma$  (top left),  $\eta^\gamma$  (top right), and  $p_T^W$  (bottom left) in  $W(\rightarrow \ell\nu) + \gamma$  process from the private aMC@NLO sample (blue) and the LO sample used for background prediction (red) along with the NLO / LO ratios.

Table 3.1: NNLO / LO correction factors for  $Z(\rightarrow \nu\bar{\nu})+\gamma$  and  $W(\rightarrow \ell\nu)+\gamma$  samples.

$E_T^\gamma$ range (GeV)	$Z(\rightarrow \nu\bar{\nu})+\gamma$	$W(\rightarrow \ell\nu)+\gamma$
[175, 190]	1.44	1.40
[190, 250]	1.41	1.37
[250, 400]	1.35	1.31
[400, 700]	1.29	1.26
[700, inf]	1.15	1.15

duced samples. (Note that the denominator cross section includes contributions from processes with up to two additional partons, and is therefore not a LO cross section in the strict sense of the word.  $V\gamma$  k-factors found in literature can be  $\gg 1$  at high  $E_T^\gamma$ , if the denominator only accounts for the cross section of  $q\bar{q} \rightarrow V\gamma$  process.)

Additionally, higher-order electroweak correction factors are also applied as a function of  $E_T^\gamma$ . Out of various electroweak higher-order effects, ones that can give sizeable ( $\gg \mathcal{O}(\alpha)$ ) corrections to the cross section are Sudakov suppression at high boson  $p_T$  and potentially the addition of photon-induced scattering processes [?, ?]. We apply the correction factors shown in Figure 3-3, which are combinations of Sudakov suppression factors and photon-induced enhancements, and are provided by the authors of Ref. [?] in addition to the NNLO QCD correction.

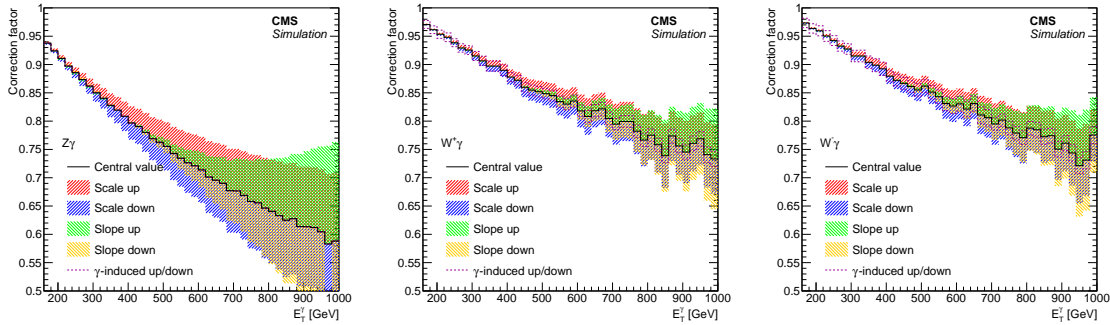


Figure 3-3: Electroweak NLO cross section corrections as a function of photon  $p_T$  for  $Z(\rightarrow \nu\bar{\nu})+\gamma$  (left),  $W^+ + \gamma$  (middle), and  $W^- + \gamma$  (right) processes, overlaid with uncertainty bands. See text for descriptions of the individual components of the uncertainty. The uncertainty due to  $\gamma$ -induced production is negligible in  $Z(\rightarrow \nu\bar{\nu})+\gamma$  production.

The differential cross section after the full higher-order corrections is therefore

denoted as

$$d\sigma^{\text{NNLO QCD+NLO EW}} = d\sigma^{\text{LO}} k^{\text{NNLO QCD}} (1 + \kappa^{\text{EW Sudakov}} + \kappa^{\text{EW}q\gamma}), \quad (3.1)$$

where  $k^{\text{NNLO QCD}} = d\sigma^{\text{NNLO QCD}}/d\sigma^{\text{LO}}$ , and the two  $\kappa$  terms are the Sudakov suppression and photon-induced enhancement components of the electroweak correction, respectively.

Furthermore, subtle differences between simulation and observation in the reconstruction and identification efficiencies for various particle candidates are accounted for with the set of selection efficiency correction factors  $\rho$ . The value of an individual  $\rho$  typically lies within a few percent of unity. Further details on the measurement and values of various  $\rho$  are found in Chapter 2.

Four sources of systematic uncertainties considered for  $E_T^\gamma$  distribution ratios of the  $V+\gamma$  processes are higher-order QCD corrections, higher-order EWK corrections, choice of PDF set, and data-to-simulation correction factors  $\rho$ . The four uncertainties are all considered as correlated between the  $E_T^\gamma$  bins.

The higher-order QCD renormalization and factorization scale uncertainties on the NNLO cross sections are assessed by varying the respective scales by factor 2 and 0.5 during the cross section computation. These uncertainties are between 7-8%, varying bin by bin, and are considered uncorrelated in the ratio between the  $Z(\rightarrow \nu\bar{\nu})+\gamma$  and  $W(\rightarrow \ell\nu)+\gamma$  processes.

Theoretical uncertainties on the electroweak corrections are not well understood to date. We estimate the magnitude of the uncertainty on  $\kappa^{\text{EW Sudakov}}$  and  $\kappa^{\text{EW}q\gamma}$  to be  $(\kappa^{\text{EW Sudakov}})^2$  and  $\kappa^{\text{EW}q\gamma}$ , i.e., square of the correction for Sudakov suppression and the 100% of the correction itself for the photon-induced enhancement. The choice of using the square of  $\kappa^{\text{EW Sudakov}}$  is motivated by the fact that fully resummed leading-log Sudakov suppression is an exponential of  $\kappa^{\text{EW Sudakov}}$ .

For the Sudakov suppression, which is the dominant term in the electroweak correction, we further consider two types of systematic variations, inspired by ref. [?], which provides a prescription for electroweak correction uncertainties for  $V + \text{jets}$

processes. In this paper, electroweak correction as a function of the boson  $p_T$  is varied in overall scale and in slope. The slope variation is realized by selecting a point in the boson  $p_T$  spectrum and letting the shift in correction cross over at the point (see Figure 3-4). Following this prescription, we let the Sudakov suppression vary in overall scale and in slope, where we choose our crossover point for the slope variation to be at  $E_T^\gamma = 590 \text{ GeV}$ .

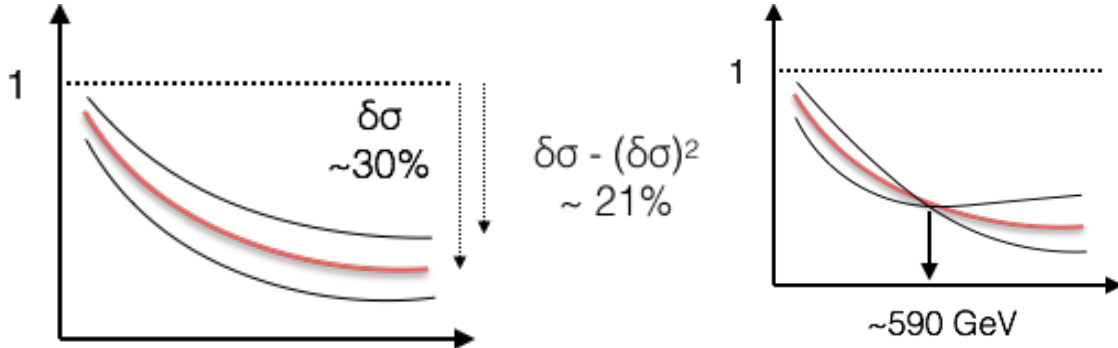


Figure 3-4: Electroweak correction variation scheme to cover the scale (left) and shape (right) uncertainties.

The PDF uncertainty is evaluated by varying the weight of each event using the weights provided in the NNPDF set, and taking the standard deviation of the resulting  $E_T^\gamma$  distributions. This uncertainty is considered fully correlated in the ratio between the  $Z(\rightarrow \nu\bar{\nu})+\gamma$  and  $W(\rightarrow \ell\nu)+\gamma$  processes, i.e., the variation of the ratio is bounded by the ratios of the upward and downward variations.

Finally, data-to-simulation correction factors  $\rho$  for the lepton identification efficiencies have associated uncertainties that do not cancel when taking ratios between regions defined by different lepton selection requirements.

### 3.2.2 Data-driven Control Regions

Contributions from the  $Z(\rightarrow \nu\bar{\nu})+\gamma$  and  $W(\rightarrow \ell\nu)+\gamma$  processes are estimated using observed data in four mutually exclusive single-electron, single-muon, dielectron, and dimuon control regions defined in Section 3.1. The ratios between the expected yields of these processes are constrained by MC simulations of  $V+\gamma$  processes. This background estimation method exploits cancellation of some of the systematic uncertain-

ties, both experimental and theoretical, in the ratios of the photon  $E_T^\gamma$  distributions of  $V+\gamma$  processes, from here on referred to as “transfer factors”.

For example, in the transfer factor between the  $Z(\rightarrow \nu\bar{\nu})+\gamma$  and  $Z(\rightarrow \ell\bar{\ell})+\gamma$  processes, denoted  $R_{\ell\ell\gamma}^{Z\gamma}$ , the uncertainties due to photon energy calibration, jet energy resolution, and higher-order QCD effects are significantly reduced compared to when such effects are considered for individual processes. The only uncertainties in the transfer factor  $R_{\ell\ell\gamma}^{Z\gamma}$  that do not largely cancel are those on lepton identification efficiency and the statistical uncertainty due to the limited MC sample size. Figure 3-5 shows the transfer factor  $R_{ee\gamma}^{Z\gamma}$  ( $R_{\mu\mu\gamma}^{Z\gamma}$ ) between the dielectron (dimuon) control region and the combined signal regions, for which the numerator is the expected  $Z(\rightarrow \nu\bar{\nu})+\gamma$  yield in the combined signal regions and the denominator is the expected  $Z(\rightarrow \ell\bar{\ell})+\gamma$  yield in the relevant control region.

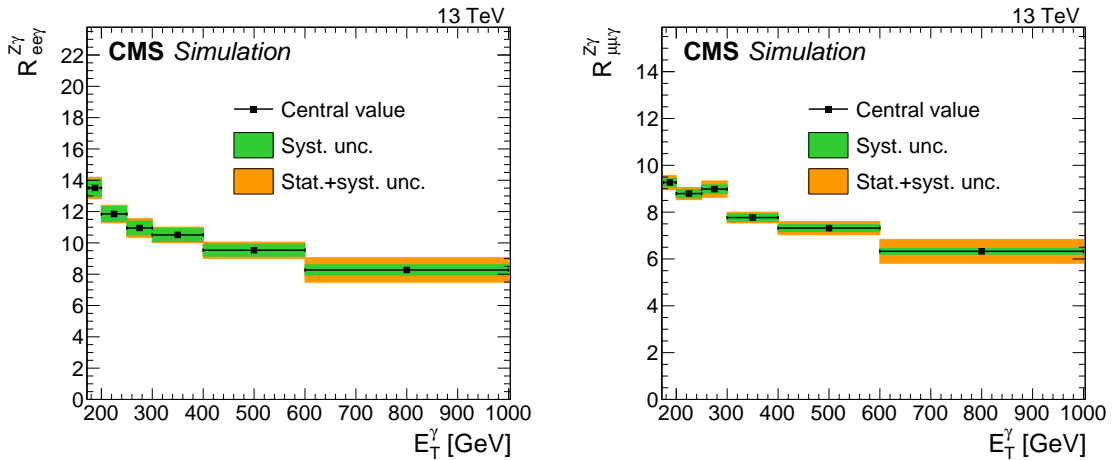


Figure 3-5: Transfer factors  $R_{ee\gamma}^{Z\gamma}$  (left) and  $R_{\mu\mu\gamma}^{Z\gamma}$  (right). The uncertainty bands in green (inner) and orange (outer) show the systematic uncertainty, and the combination of systematic and statistical uncertainty arising from limited MC sample size, respectively. The systematic uncertainties considered are the uncertainties in the data-to-simulation correction factors  $\rho$  for the lepton identification efficiencies.

For increasing  $E_T^\gamma$ , the  $Z$  boson in a  $Z(\rightarrow \ell\bar{\ell})+\gamma$  event tends to emerge with lower rapidity, and hence so do its decay products. As a consequence, the charged leptons are more likely to fall within the inner tracker acceptance, which increases the dilepton control region selection efficiency of these events. In contrast, the signal

region selection efficiency of  $Z(\rightarrow \nu\bar{\nu})+\gamma$  events is unaffected by the rapidity of the final state neutrinos, as long as the observed  $E_T^{\text{miss}}$  has the appropriate magnitude and azimuthal direction. This causes the distinctive drop in the ratio  $R_{\ell\ell\gamma}^{Z\gamma}$  with increasing  $E_T^\gamma$ .

Using the transfer factor  $R_{\ell\ell\gamma}^{Z\gamma}$ , the total estimated event yield  $T_{\ell\ell\gamma}$  in each dilepton control region in the  $i^{\text{th}}$  bin of the  $E_T^\gamma$  distribution can be expressed as

$$T_{\ell\ell\gamma,i} = \frac{N_i^{Z\gamma}}{R_{\ell\ell\gamma,i}^{Z\gamma}} + b_{\ell\ell\gamma,i}, \quad (3.2)$$

where  $N^{Z\gamma}$  is the number of  $Z(\rightarrow \nu\bar{\nu})+\gamma$  events in the combined signal regions and  $b_{\ell\ell\gamma}$  is the predicted contribution from other background sources in the dilepton control region, namely  $t\bar{t}\gamma$ ,  $VV\gamma$ , and misidentified hadrons. The subscript  $i$  indicates that the quantities are evaluated in bin  $i$  of the  $E_T^\gamma$  distribution.

Similar considerations apply to events arising from  $W(\rightarrow \ell\nu)+\gamma$  processes. A large fraction of such events are rejected by the electron and muon vetoes in the signal region selection and end up in the control regions instead. However, hadronic tau events and events where the leptons are out of acceptance or fail to be reconstructed will remain in the signal region, on top of the vetoes having imperfect efficiencies. In the ratio of these two classes of events, denoted  $R_{\ell\gamma}^{W\gamma}$ , the only uncertainties that remain non-negligible are those associated with the lepton identification efficiency and the MC statistical uncertainty.

Table 3.2 gives the breakdown of the  $W(\rightarrow \ell\nu)+\gamma$  background passing the full event selection for the signal region, categorized by the lepton flavor and, for the case of electrons and muons, the lepton pseudorapidity at the parton-level. From this breakdown, one sees that events where the  $W$  boson decays to a  $\tau$  and a neutrino constitutes approximately 60% of the  $W(\rightarrow \ell\nu)+\gamma$  background. The remaining 40% of the  $W(\rightarrow \ell\nu)+\gamma$  background comes from events where  $W$  boson decays to a  $\mu$  or  $e$  and a neutrino. Events containing an electron are more likely to be within the detector acceptance, while those with a muon are more likely to be out of acceptance. For the in-acceptance background ( $|\eta| < 2.5$ ), the identification efficiency, which is lower

Table 3.2: The breakdown of simulated  $W + \gamma$  events passing the full event selection. Events are categorized in the  $W$  decay mode. Events with  $e$  and  $\mu$  final states are further divided into those where the lepton was roughly within acceptance ( $|\eta| < 2.5$ ) but failed the lepton veto, and those where the lepton was out of acceptance ( $|\eta| > 2.5$ ). For each  $W$  decay mode, the fraction out of total generated ( $A \times \epsilon$ ) is shown.

Subprocess	$A \times \epsilon \times 10^3$
$W \rightarrow e + \gamma$	1.68
$ \eta^e  < 2.5$	1.35
$ \eta^e  > 2.5$	0.32
$W \rightarrow \mu + \gamma$	1.83
$ \eta^\mu  < 2.5$	0.74
$ \eta^\mu  > 2.5$	1.08
$W \rightarrow \tau + \gamma$	5.03

for electrons than for muons, which translates to a larger background contribution from the electrons. Meanwhile, the  $E_T^{\text{miss}}$  requirement explains the behavior of the out-of-acceptance background ( $|\eta| > 2.5$ ). A large fraction of electrons that are out of tracker acceptance are still captured by the calorimeters, while out-of-acceptance muons directly contribute to missing momentum leading to a larger background contribution from muons.

Figure 3-6 shows the transfer factor  $R_{e\gamma}^{W\gamma}$  ( $R_{\mu\gamma}^{W\gamma}$ ) between the single-electron (single-muon) control region and the combined signal regions, for which the numerator is the estimated  $W(\rightarrow \ell\nu) + \gamma$  yield in the combined signal regions, and the denominator is the estimated  $W(\rightarrow \ell\nu) + \gamma$  yield in the relevant control region. The ratio  $R_{e\gamma}^{W\gamma}$  decreases with increasing  $E_T^\gamma$  in a similar manner to  $R_{\ell\ell\gamma}^{Z\gamma}$ . The underlying logic is the same; e.g., that the signal region selection efficiency is unaffected by  $E_T^\gamma$  while the control region acceptances increase with increasing  $E_T^\gamma$  due to increased lepton efficiency resulting from lower  $W$  rapidity.

Finally, to benefit further from the larger statistical power that the single-lepton control samples provides, an additional transfer factor  $f_{W\gamma}^{Z\gamma} = N^{Z\gamma}/N^{W\gamma}$  is defined to connect the  $Z(\rightarrow \nu\bar{\nu}) + \gamma$  and  $W(\rightarrow \ell\nu) + \gamma$  background yields in the signal regions, where the quantity  $N^{W\gamma}$  is the number of  $W(\rightarrow \ell\nu) + \gamma$  events in the combined signal regions. When calculating the ratio  $f_{W\gamma}^{Z\gamma}$ , all experimental uncertainties associated

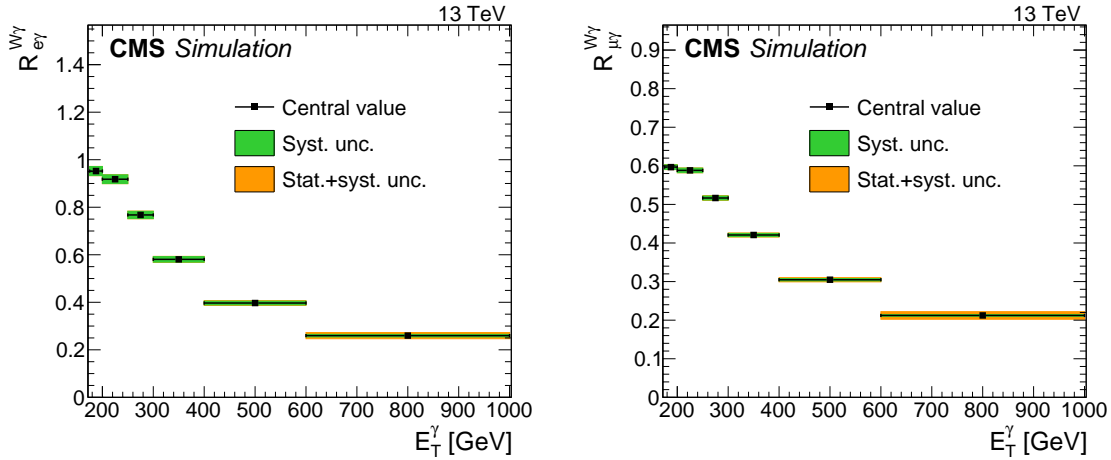


Figure 3-6: Transfer factors  $R_{e\gamma}^{W\gamma}$  (left) and  $R_{\mu\gamma}^{W\gamma}$  (right). The uncertainty bands in green (inner) and orange (outer) show the systematic uncertainty, and the combination of systematic and statistical uncertainty arising from limited MC sample size, respectively. The systematic uncertainties considered are the uncertainties in the data-to-simulation correction factors  $\rho$  for the lepton identification efficiencies.

with the data-to-simulation correction factors  $\rho$  cancel since both processes result in very similar event configurations. The main uncertainties in  $f_{W\gamma}^{Z\gamma}$  are those from higher-order theoretical corrections, discussed in Section 3.2.1. Figure 3-7 shows the effect of each systematic uncertainty in  $f_{W\gamma}^{Z\gamma}$  with respects to its nominal value for  $Z(\rightarrow \nu\bar{\nu})+\gamma$  and  $W(\rightarrow \ell\nu)+\gamma$  respectively.

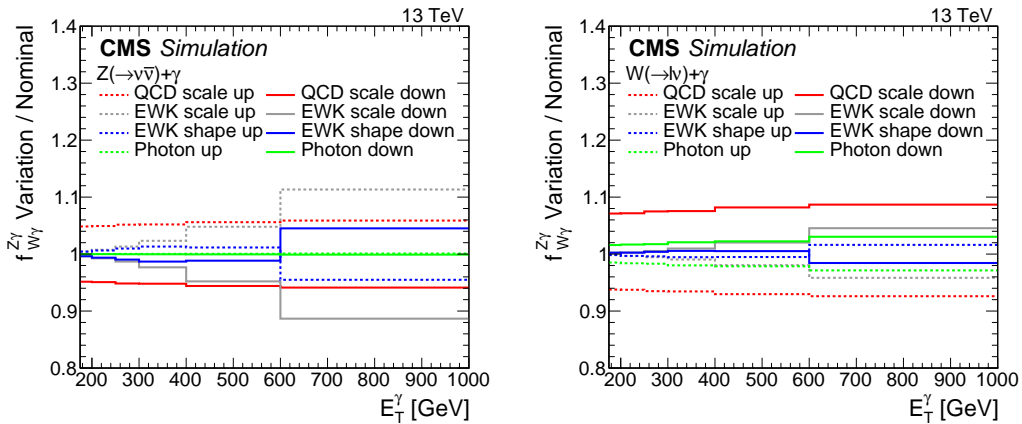


Figure 3-7: Systematic uncertainty in the transfer factors for  $Z(\rightarrow \nu\bar{\nu})+\gamma$  (left) and  $W(\rightarrow \ell\nu)+\gamma$  (right). The last bin includes all events with  $E_T^\gamma > 1000$  GeV.

The ratio  $f_{W\gamma}^{Z\gamma}$  rises rather than falls with increasing  $E_T^\gamma$  because  $W(\rightarrow \ell\nu)+\gamma$

events have a lower rather than higher signal region selection efficiency if the charged lepton falls within the tracker acceptance while the  $Z(\rightarrow \nu\bar{\nu})+\gamma$  efficiency is independent of  $E_T^\gamma$ . Figure 3-8 shows the transfer factor  $f_{W\gamma}^{Z\gamma}$  between the  $Z(\rightarrow \nu\bar{\nu})+\gamma$  and  $W(\rightarrow \ell\nu)+\gamma$  processes in the combined signal region.

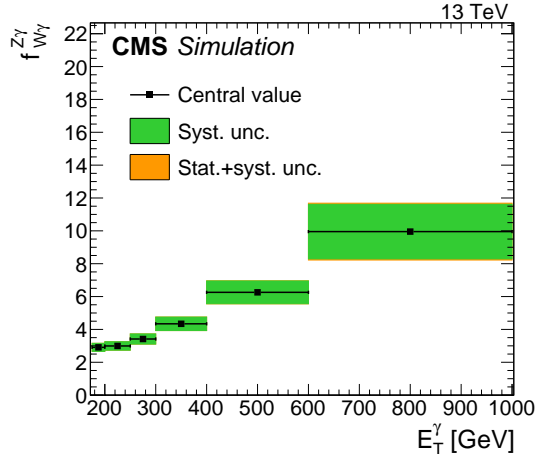


Figure 3-8: Transfer factor  $f_{W\gamma}^{Z\gamma}$ . The uncertainty bands in green (inner) and orange (outer) show the systematic uncertainty, and the combination of systematic and statistical uncertainty arising from limited MC sample size, respectively. The systematic uncertainties considered are the uncertainties from higher-order theoretical corrections.

Using  $R_{\ell\gamma}^{W\gamma}$  and  $f_{W\gamma}^{Z\gamma}$ , the total estimated event yield  $T_{\ell\gamma}$  in each single-lepton control region in the  $i^{\text{th}}$  bin of the  $E_T^\gamma$  distribution can be expressed as

$$T_{\ell\gamma,i} = \frac{N_i^{Z\gamma}}{R_{\ell\gamma,i}^{W\gamma} f_{W\gamma,i}^{Z\gamma}} + b_{\ell\gamma,i}, \quad (3.3)$$

where  $b_{\ell\gamma}$  is the predicted contribution from other background sources in the single-lepton regions, namely misidentified electrons and hadrons and other minor SM processes.

### 3.3 Misidentified electrons

An electron can be misidentified as a photon if the association of tracks or track seeds to the supercluster in ECAL fails in the reconstruction step. The production of

a single  $W$  boson decaying to an electron and a neutrino is a high-rate process, and it mimicks the photon plus  $E_T^{\text{miss}}$  signature if the electron is misidentified.

The rate at which this misidentification occurs is proportional to the inefficiency  $1 - \epsilon_e^{\text{track}}$  of the tracking, defined over the electrons passing the photon identification criteria described in Sec. 1.4 except the electron veto. This partial identification is denoted as  $e\gamma$  ID in the following. If one assumes that the kinematic and other critical properties of the electron plus  $E_T^{\text{miss}}$  events are unaffected by the electron misidentification, it is possible to model the electron misidentification background by taking a proxy sample with well-identified electrons and scaling this sample by  $R_e = (1 - \epsilon_e^{\text{track}})/\epsilon_e^{\text{track}}$ .

The “tag-and-probe” method described in Section 2.2.1 with appropriate changes is used to measure the efficiency corresponding to the factor  $R_e$  in data.

The first such change is that the sample is split into  $e\gamma$  and  $ee$  categories depending on whether the probe passes or fails the electron veto requirement. Probes in both categories must also pass the  $e\gamma$  ID. Denoting the area of the peak in each category  $N_{e\gamma}$  and  $N_{ee}$ , respectively, the ratio  $N_{e\gamma}/N_{ee}$  is equal to  $R_e$  up to minor systematic corrections.

The second such change is in the background model used in the TP fits. The backgrounds to the  $e\gamma$  fit consist of processes with actual electron and photon in the final state, such as  $W\gamma$  and  $Z \rightarrow ee$  with a hard radiation off one of the electrons. Because of this, we scale the mass distribution of the  $\mu + \gamma$  sample by the ratio of electron-probe to muon-probe events taken from MC to account for the different rates of FSR and bremsstrahlung between muons and electrons. As an alternative template to assess the systematic effect introduced by the choice of the background template, the unscaled mass distribution is also tested.

Figure 3-9 shows the six fits performed on  $ee$  and  $e\gamma$  in bins of probe  $p_T$ , from which the  $R_e$  factor used for the estimation of the electron misidentification background is derived.

The proxy sample for the background estimation is obtained by identical event selection as that described in Sec. 3.1, but with the pixel-seed veto inverted on the

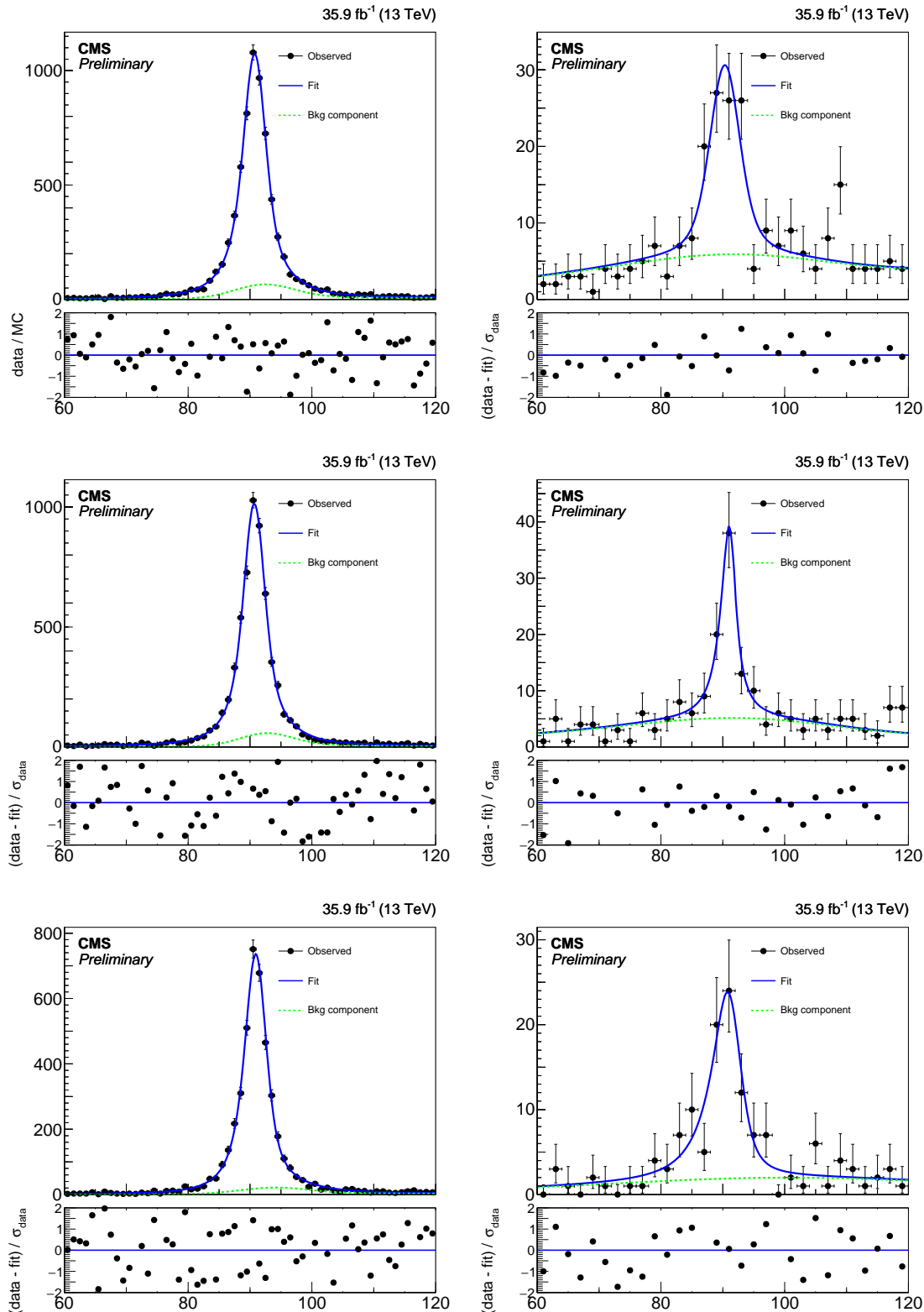


Figure 3-9: Fits to the mass distributions for  $ee$  (left) and  $e\gamma$  (right) selections, in bins of probe  $p_T$ :  $175 < p_T < 200 \text{ GeV}$  (top),  $200 < p_T < 250 \text{ GeV}$  (middle),  $p_T > 250 \text{ GeV}$  (bottom). The blue solid line represents the full fit model, and the green dashed line its background component.

photon candidate object.

Figure 3-10 shows the derived  $R_e$  factor as a function of  $E_T^\gamma$ . The electron proxy sample is reweighted by  $R_e$  depending on the  $p_T$  of the electron object.

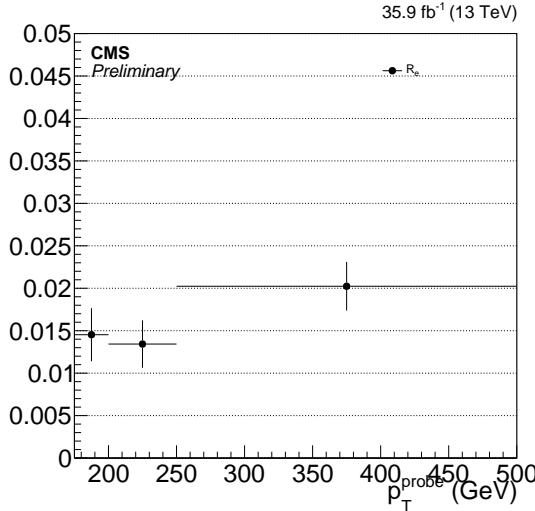


Figure 3-10: Electron to photon fake rate  $R_e$ .

### 3.4 Misidentified hadrons

The estimation of hadron misidentification background proceeds in multiple steps. First, the fraction of hadronic objects within a pool of photon candidate objects in the photon plus jet control region is measured. This measurement is described in detail in Section 2.2.2. Figure 3-11 and Table 3.3 show the final impurity and associated uncertainties as a function of  $p_T$ .

$p_T$ (GeV)	Nominal	Sources of Systematic Uncertainty				
		Sideband	CH	Iso	Shape	Bgkd. Stats
(175, 200)	$4.31 \pm 0.21$	0.09	0.18	0.05	0.04	
(200, 250)	$3.39 \pm 0.17$	0.01	0.16	0.06	0.03	
(250, 300)	$2.44 \pm 0.22$	0.14	0.16	0.06	0.05	
(300, 350)	$1.99 \pm 0.23$	0.12	0.16	0.07	0.08	
(350, 400)	$1.43 \pm 0.28$	0.23	0.11	0.05	0.10	
(400, $\infty$ )	$0.63 \pm 0.30$	0.27	0.09	0.05	0.05	

Table 3.3: Impurities for photons as a function of  $p_T$ .

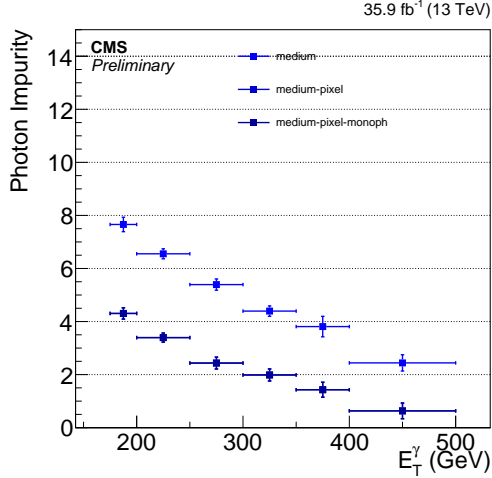


Figure 3-11: Impurities for photons as a function of  $p_{\text{T}}$ . The different bands show the effects of adding different stages of the full ID, starting with the baseline ID and isolation and successively adding the pixel seed veto.

Following this measurement, another control sample is formed where the photon in the photon plus jet sample is replaced by a hadronic proxy object. The hadronic proxy object is a reconstructed photon object which pass the photon ID described in Section 1.4 with the exception of failing at least one of the following cuts:

- $\sigma_{i\eta i\eta} < 0.01022$
- PF Charged Hadron isolation  $< 0.441 \text{ GeV}$ .

Additionally, we apply a  $E_{\text{T}}^{\text{miss}} < 60 \text{ GeV}$  cut to make this region orthogonal to the signal region of the analysis.

The hadronic transfer factor  $R_h$ , which measures the rate at which hadronic proxy objects result in hadrons that are misidentified as candidate photons, is obtained by dividing the estimated number of misidentified hadrons in the photon plus jet sample by the number of events in the hadron proxy + jet control region as a function of  $p_{\text{T}}$ . Figure 3-12 shows the transfer factor  $R_h$  along with the various distributions used for its derivation.

Finally, a third control sample of events with a hadronic proxy object and  $E_{\text{T}}^{\text{miss}} > 170 \text{ GeV}$  is prepared. Under the assumption that the  $R_h$  stays constant regardless of whether the event has a high- $p_{\text{T}}$  jet or  $E_{\text{T}}^{\text{miss}}$ , this proxy plus  $E_{\text{T}}^{\text{miss}}$  sample is

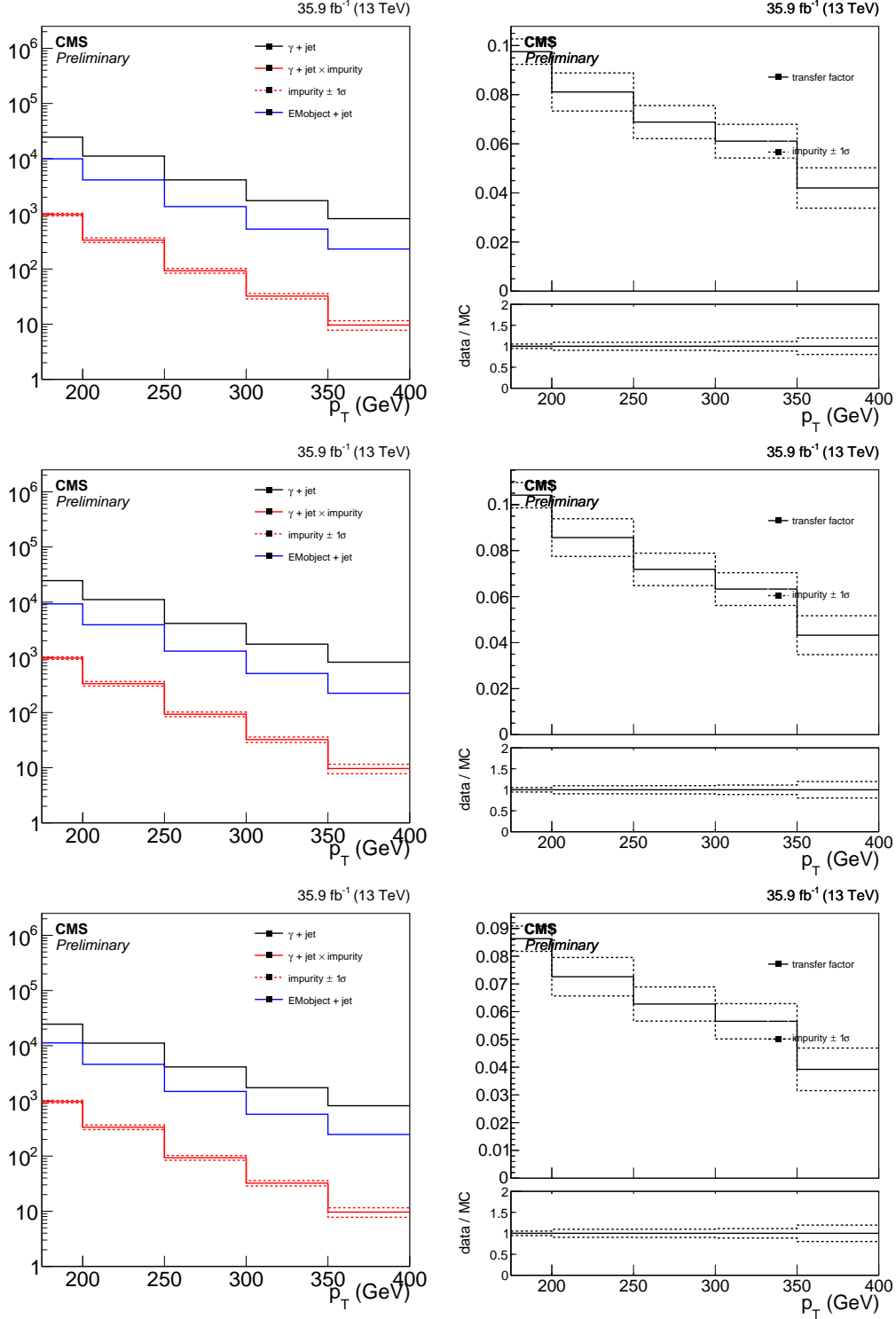


Figure 3-12: Left: The  $p_T$  distribution of the candidate photon object in the photon + jet control sample (black), the result of scaling it with the impurity (red), and the  $p_T$  distribution of the hadronic proxy object in the proxy + jet control sample (blue). Right: Hadronic transfer factor  $R_h$ , which is the ratio of the red and blue distributions in the left plot. Top: Nominal hadron proxy object. Middle: Tighter hadron proxy object. Bottom: Looser hadron proxy object.

then weighted by  $R_h$  to arrive at an estimate of the misidentified hadron plus  $E_T^{\text{miss}}$  background of this analysis.

To estimate the uncertainty on this background, we repeat the above method using tighter and looser definitions of the hadron proxy object. The tighter definition differs from the nominal by the following cuts:

- $\rho$ -corrected PF Neutral Hadron isolation  $< 0.264 + 0.014 \times p_T^\gamma + 0.000019 \times (p_T^\gamma)^2$ .
- $\rho$ -corrected PF Photon isolation  $< 2.362 + 0.0053 \times p_T^\gamma$ ,

and the looser definition differs from the nominal by the following cuts:

- $\rho$ -corrected PF Neutral Hadron isolation  $< 10.910 + 0.014 \times p_T^\gamma + 0.000019 \times (p_T^\gamma)^2$ .
- $\rho$ -corrected PF Photon isolation  $< 3.630 + 0.0053 \times p_T^\gamma$ .

The different distributions from the nominal, tight, and loose selections are shown in Figure 3-13. The tight and loose shapes are taken as the one sigma band around the nominal estimate. Additionally, there is an uncertainty coming from the estimation of the photon purity. Figure 3-14 shows the resulting shapes from moving the shapes generated by a one sigma shift in the purity.

### 3.5 Beam halo

Based on the beam halo features discussed in Section 1.9, a two-template fit to the  $\phi'$  distribution of the photons in the candidate sample, where the templates are that of the halo shower and a uniform distribution, accurately estimates the amount of beam halo background present in the signal region. For this analysis, the splitting of the signal region functions in a similar manner, enabling us to determine the beam halo contribution during the signal extraction procedure.

In the horizontal ( $H$ ) and vertical ( $V$ ) signal regions, collision processes occupy the relative fractions of phase space  $C_H = 1/\pi$  and  $C_V = (\pi - 1)/\pi$ , respectively. The corresponding fractions for beam halo events are determined by selecting a halo-enriched sample where the halo identification is inverted. Thus, a fit of the two

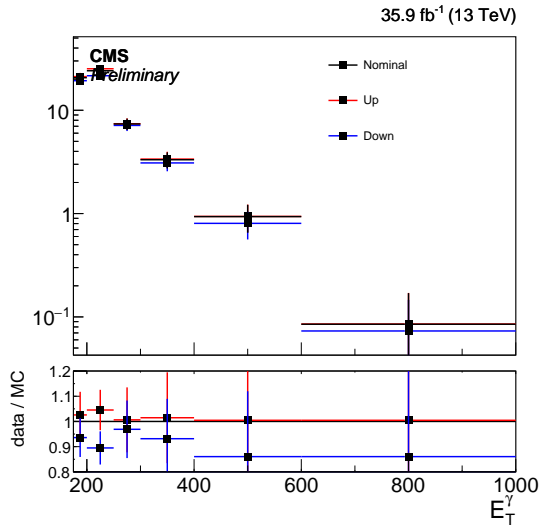


Figure 3-13: The  $p_T$  distribution of the estimated contribution from hadronic fakes in the signal region. The distribution labeled Up (Down) comes from the tighter (looser) selection. The systematic uncertainty resulting from this variation is around 5% at the low end of our  $p_T$  range and increases to 15% after  $p_T > 400$  GeV.

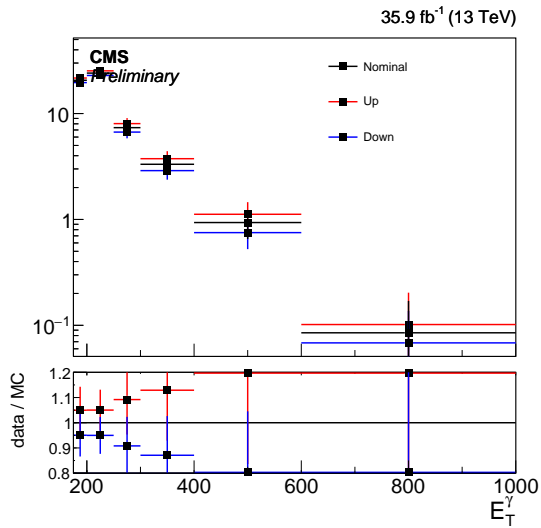


Figure 3-14: The  $p_T$  distribution of the estimated contribution from hadronic fakes in the signal region. The distribution labeled Up (Down) comes from varying the purity one sigma up (down). The systematic uncertainty resulting from this variation is around 5% at the low end of the  $p_T$  range and increases to 20% after  $p_T > 400$  GeV.

signal regions provides an estimate of the overall normalization of the beam halo background, denoted  $h$ .

The  $E_T^\gamma$  dependence of the halo background is encoded in  $n_{K,i}^{\text{halo}}$ , the unit-normalized beam halo prediction in the  $i^{\text{th}}$  bin of the signal region  $K \in \{H, V\}$ . Using the notation introduced in Section 3.2, the total estimated background  $T_K$  in the two signal regions are

$$\begin{aligned} T_{K,i} &= C_K(N_i^{Z\gamma} + N_i^{W\gamma}) + hn_{K,i}^{\text{halo}} + C_K b_{K,i} \\ &= C_K(1 + f_{W\gamma i}^{Z\gamma -1})N_i^{Z\gamma} + hn_{K,i}^{\text{halo}} + C_K b_{K,i}, \end{aligned} \quad (3.4)$$

where  $b_{K,i}$  is the total contribution to bin  $i$  of region  $K$  from electron and hadron misidentification, ECAL spikes, and other minor SM background processes.

## 3.6 Spikes

Given the observations in Section 1.10, the time distribution of spike-like rec hits outside of the window  $-15 < t < -10$  ns (and the equivalent with one-bunch-crossing shift) is understood to be due to delayed interactions of neutral hadrons with the APDs, as documented also in Ref. [?]. In other words, ECAL spike clusters which survive the time cleaning cut of the standard reconstruction are a part of a broad tail of a distribution, and there is no evidence of spike signals that specifically populate the “in-time” region  $-3 < t < 3$  ns.

Having established that there is no special population of ECAL spikes in the in-time region, we can estimate the number of ECAL spike events present in the signal candidate sample by an “ABCD” method, where

- A = Number of clusters with  $\sigma_{i\eta i\eta}$  or  $\sigma_{i\phi i\phi}$  less than 0.001 and seed time  $-15 < t < -10$  ns, counted in the special-reconstruction sample,
- B = Number of clusters with both  $\sigma_{i\eta i\eta}$  and  $\sigma_{i\phi i\phi}$  greater than 0.001 and seed time  $-15 < t < -10$  ns, counted in the special-reconstruction sample,

- C = Number of clusters with  $\sigma_{i\eta i\eta}$  or  $\sigma_{i\phi i\phi}$  less than 0.001 but an in-time seed, counted in the standard-reconstruction sample passing all other signal event selection,

and D is the estimated number of spike events in the signal region, obtained by

$$D = C \times \frac{B}{A}. \quad (3.5)$$

The special-reconstruction samples for A and B are from the SinglePhoton datasets, with only the timing cleaning removed from the offline reconstruction. In this way, the selection bias over spikes from the L1T, HLT, and offline reconstruction is equally applied to samples A, B, and C.

Plugging in the observed numbers, we have

$$A = 4969$$

$$B = 1180$$

$$C = 54$$

$$D = 12.8 \pm 1.8(\text{stat.})$$

There are, however, at least two reasons to believe that this method overestimates the number of spike events in the signal region. One is that the population C contains some physical, prompt photon clusters that just happens to be narrow, as observed in Fig. 1-14. Another reason is that there is likely a correlation between the cluster width and the seed time such that the ratio of true D to C is smaller than  $B/A$ . This statement is based on the standard hypothesis that the wide-cluster spike is an ECAL spike embedded in a physical EM shower cluster. Under this model, spikes in wide clusters are mainly caused by prompt neutral hadrons in a jet, which implies that they strongly prefer seed time  $-15 < t < -10$  ns. Given that this is a minor background with a relatively large uncertainty, as described below, we will still use this estimate as the nominal value of predicted spike contribution in the signal region.

The uncertainty in the estimate of D is evaluated by two modifications to A, B,

and C. First, the three values are recomputed with using  $\sigma_{in in} < 0.001$  as the only definition of narrow cluster. This results in a minor change of the value of D of  $12.1 \pm 1.7$ . Next, A and B are computed using a lower- $p_T$  SinglePhoton sample, requiring triggers Photon135\_PFMET100 or Photon120\_R9Id90\_HE10\_IsoM to have fired, instead of the signal trigger. The second modification gives  $D = 9.1 \pm 1.3$ . We then take twice the discrepancy between the nominal D and the D value from the second modification as the systematic uncertainty in the spike background estimate.

### 3.7 Statistical Interpretation

The potential signal contribution is extracted from the data via simultaneous fits to the  $E_T^\gamma$  distributions in the signal and control regions defined in Section 3.1. Uncertainties in various quantities are represented by nuisance parameters in the fit. Predictions for  $Z(\rightarrow \nu\bar{\nu}) + \gamma$ ,  $W(\rightarrow \ell\nu) + \gamma$ , and the beam halo backgrounds are varied in the fit. Beam halo is not a major background, but the extraction of its rate requires a fit to the observed distributions in the signal region.

Free parameters of the fit are the yield of  $Z(\rightarrow \nu\bar{\nu}) + \gamma$  background in each bin of the signal regions ( $N_i^{Z\gamma}$ ) and the overall normalization of the beam halo background ( $h$ ). Bin-by-bin yields of  $W(\rightarrow \ell\nu) + \gamma$  and  $Z(\rightarrow \ell\bar{\ell}) + \gamma$  samples in all regions are related to the yield of  $Z(\rightarrow \nu\bar{\nu}) + \gamma$  through the MC prediction through the transfer factors defined in Section 3.2. The transfer factors are allowed to shift within the aforementioned theoretical and experimental uncertainties.

The background-only likelihood that is maximized in the fit is

$$\begin{aligned}
\mathcal{L} &= \prod_i \{\mathcal{L}_{\text{signal}} \times \mathcal{L}_{\text{single-lepton}} \times \mathcal{L}_{\text{dilepton}}\} \times \mathcal{L}_{\text{nuisances}} \\
&= \prod_i \left\{ \prod_{K=H,V} \mathcal{P}(d_{K,i} | T_{K,i}(\vec{\theta})) \times \prod_{\ell=e,\mu} \mathcal{P}(d_{\ell\gamma,i} | T_{\ell\gamma,i}(\vec{\theta})) \times \prod_{\ell=e,\mu} \mathcal{P}(d_{\ell\ell\gamma,i} | T_{\ell\ell\gamma,i}(\vec{\theta})) \right\} \times \prod_j \mathcal{N}(\theta_j) \\
&= \prod_i \left\{ \begin{array}{l} \prod_{K=H,V} \mathcal{P}\left(d_{K,i} \left| \left(1 + f_{W\gamma,i}^{Z\gamma}{}^{-1}(\vec{\theta})\right) C_K N_i^{Z\gamma} + h n_{K,i}^{\text{halo}}(\vec{\theta}) + C_K b_{K,i}(\vec{\theta})\right)\right. \\ \quad \times \prod_{\ell=e,\mu} \mathcal{P}\left(d_{\ell\gamma,i} \left| \frac{N_i^{Z\gamma}}{R_{\ell\gamma,i}^{W\gamma}(\vec{\theta}) f_{W\gamma,i}^{Z\gamma}(\vec{\theta})} + b_{\ell\gamma,i}(\vec{\theta})\right.\right) \\ \quad \times \prod_{\ell=e,\mu} \mathcal{P}\left(d_{\ell\ell\gamma,i} \left| \frac{N_i^{Z\gamma}}{R_{\ell\ell\gamma,i}^{Z\gamma}(\vec{\theta})} + b_{\ell\ell\gamma,i}(\vec{\theta})\right.\right) \end{array} \right\} \times \prod_j \mathcal{N}(\theta_j), \tag{3.6}
\end{aligned}$$

following the notation introduced in Section 3.2, and where  $\mathcal{P}(n|\lambda)$  is the Poisson probability of  $n$  for mean  $\lambda$ ,  $\mathcal{N}$  denotes the unit normal distribution, and  $d_{X,i}$  is the observed number of events in bin  $i$  of region  $X$ . Systematic uncertainties are treated as nuisance parameters in the fit and are represented by  $\vec{\theta}$ . Each quantity  $Q_j$  with a nominal value  $\bar{Q}_j$  and a standard deviation of the systematic uncertainty  $\sigma_j$  appears in the likelihood function as  $\bar{Q}_j \exp(\sigma_j \theta_j)$ .

## 3.8 Results

### 3.8.1 Pre-fit and post-fit distributions

Figure 3-15 shows the observed  $E_T^\gamma$  distributions in the four control regions compared with the results from simulations before and after performing the simultaneous fit across all the control samples and signal region, and assuming absence of any signal. Figure 3-16 shows the observed  $E_T^\gamma$  distributions in the horizontal and vertical signal regions compared with the results from simulations before and after performing a combined fit to the data in all the control samples and the signal region. The observed distributions are in agreement with the prediction from SM and noncollision backgrounds.

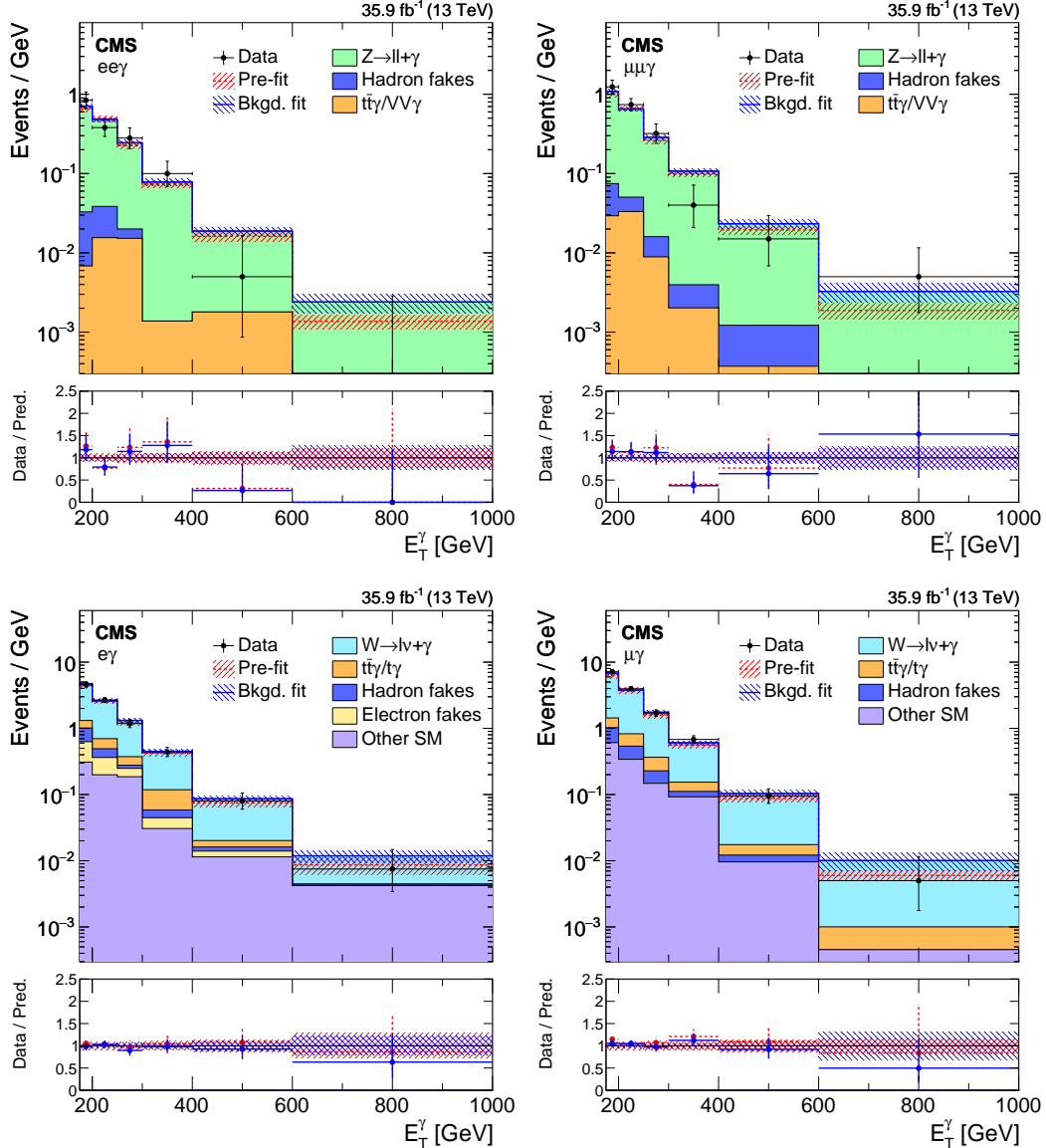


Figure 3-15: Comparison between data and MC simulation in the four control regions:  $ee\gamma$  (upper left),  $\mu\mu\gamma$  (upper right),  $e\gamma$  (lower left),  $\mu\gamma$  (lower right) before and after performing the simultaneous fit across all the control samples and signal region, and assuming absence of any signal. The last bin of the distribution includes all events with  $E_T^\gamma > 1000$  GeV. The ratios of data with the pre-fit background prediction (red dashed) and post-fit background prediction (blue solid) are shown in the lower panels. The bands in the lower panels show the post-fit uncertainty after combining all the systematic uncertainties.

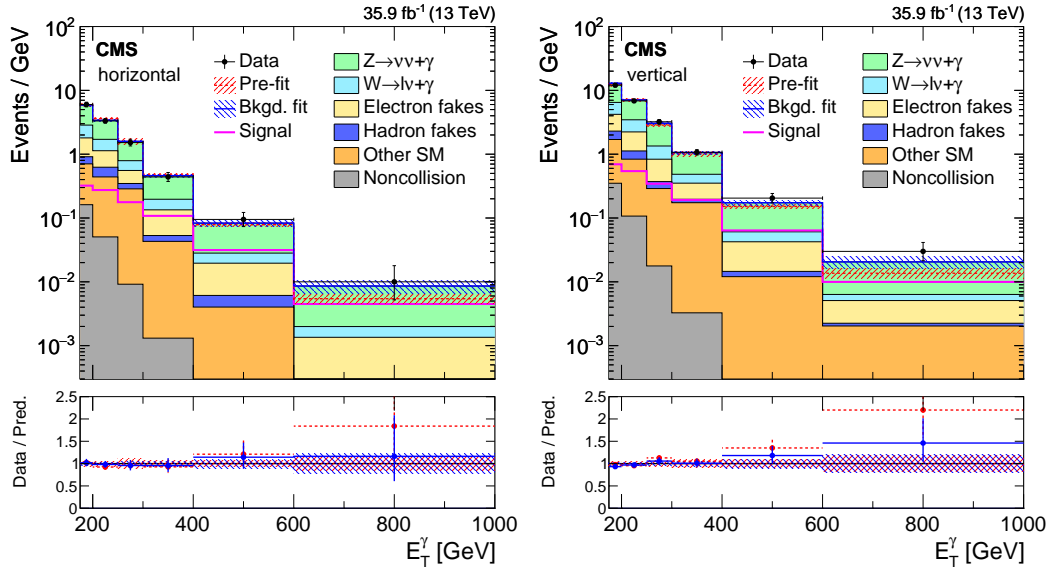


Figure 3-16: Observed  $E_T^\gamma$  distributions in the horizontal (left) and vertical (right) signal regions compared with the post-fit background expectations for various SM processes. The last bin of the distribution includes all events with  $E_T^\gamma > 1000$  GeV. The expected background distributions are evaluated after performing a combined fit to the data in all the control samples and the signal region. The ratios of data with the pre-fit background prediction (red dashed) and post-fit background prediction (blue solid) are shown in the lower panels. The bands in the lower panels show the post-fit uncertainty after combining all the systematic uncertainties. The expected signal distribution from a 1 TeV vector mediator decaying to 1 GeV DM particles is overlaid.

Table 3.4: Expected event yields in each  $E_T^\gamma$  bin for various background processes in the horizontal signal region. The background yields and the corresponding uncertainties are obtained after performing a combined fit to data in all the control samples, excluding data in the signal region. The observed event yields in the horizontal signal region are also reported.

$E_T^\gamma$ [GeV]	[175, 200]	[200, 250]	[250, 300]	[300, 400]	[400, 600]	[600, 1000]
$Z\gamma$	$81.2 \pm 8.0$	$88.2 \pm 8.4$	$38.8 \pm 4.8$	$26.8 \pm 3.7$	$8.8 \pm 1.9$	$1.4 \pm 0.7$
$W\gamma$	$27.9 \pm 3.7$	$29.9 \pm 3.9$	$11.4 \pm 1.7$	$6.3 \pm 1.2$	$1.4 \pm 0.4$	$0.1 \pm 0.1$
Misid. electrons	$22.5 \pm 2.7$	$25.7 \pm 2.7$	$10.5 \pm 1.0$	$8.2 \pm 0.7$	$2.7 \pm 0.2$	$0.5 \pm 0.0$
Misid. hadrons	$5.2 \pm 2.2$	$9.3 \pm 1.8$	$3.1 \pm 0.7$	$1.0 \pm 0.3$	$0.4 \pm 0.1$	$0.0 \pm 0.0$
Other SM	$13.6 \pm 2.0$	$19.6 \pm 1.3$	$13.9 \pm 0.4$	$4.2 \pm 0.2$	$0.8 \pm 0.0$	$0.1 \pm 0.0$
ECAL spikes	$4.3 \pm 1.3$	$2.7 \pm 0.8$	$0.5 \pm 0.1$	$0.1 \pm 0.0$	$0.0 \pm 0.0$	$0.0 \pm 0.0$
Total prediction	$154.6 \pm 8.3$	$175.4 \pm 8.8$	$78.2 \pm 5.3$	$46.6 \pm 4.0$	$14.1 \pm 2.1$	$2.1 \pm 0.8$
Observed	$150 \pm 12$	$166 \pm 13$	$76.0 \pm 8.7$	$44.0 \pm 6.6$	$19.0 \pm 4.4$	$4.0 \pm 2.0$

Table 3.5: Expected event yields in each  $E_T^\gamma$  bin for various background processes in the vertical signal region. The background yields and the corresponding uncertainties are obtained after performing a combined fit to data in all the control samples, excluding data in the signal regions. The observed event yields in the vertical signal region are also reported.

$E_T^\gamma$ [GeV]	[175, 200]	[200, 250]	[250, 300]	[300, 400]	[400, 600]	[600, 1000]
$Z\gamma$	$172 \pm 17$	$190 \pm 18$	$83 \pm 10$	$58.6 \pm 7.9$	$18.0 \pm 3.9$	$3.1 \pm 1.6$
$W\gamma$	$59.9 \pm 7.8$	$63.6 \pm 7.8$	$24.6 \pm 3.5$	$13.4 \pm 2.4$	$3.0 \pm 0.8$	$0.3 \pm 0.2$
Misid. electrons	$48.4 \pm 5.6$	$56.2 \pm 5.1$	$23.4 \pm 1.8$	$15.7 \pm 1.4$	$5.6 \pm 0.4$	$1.2 \pm 0.1$
Misid. hadrons	$15.1 \pm 4.4$	$14.5 \pm 3.1$	$4.2 \pm 0.8$	$2.3 \pm 0.8$	$0.5 \pm 0.1$	$0.1 \pm 0.1$
Other SM	$33.8 \pm 4.1$	$36.6 \pm 2.7$	$13.6 \pm 0.5$	$17.1 \pm 0.6$	$2.4 \pm 0.1$	$0.8 \pm 0.0$
ECAL spikes	$9.3 \pm 2.8$	$5.7 \pm 1.7$	$0.9 \pm 0.3$	$0.3 \pm 0.1$	$0.0 \pm 0.0$	$0.0 \pm 0.0$
Total prediction	$339 \pm 18$	$366 \pm 19$	$150 \pm 11$	$107.5 \pm 8.7$	$29.6 \pm 4.3$	$5.4 \pm 1.7$
Observed	$301 \pm 17$	$342 \pm 19$	$161 \pm 13$	$107 \pm 10$	$41.0 \pm 6.4$	$12.0 \pm 3.5$

The expected yields in each bin of  $E_T^\gamma$  for all backgrounds in the horizontal and vertical signal regions after performing a combined fit to data in all the control samples, excluding data in the signal regions, are given in Tables 3.4 and 3.5, respectively. The covariances between the predicted background yields across all the  $E_T^\gamma$  bins in the two signal regions are shown in Fig. 3-17. The expected yields together with the covariances can be used with the simplified likelihood approach detailed in Ref. [?] to reinterpret the results for models not studied in this thesis

### 3.8.2 Limits

No significant excess of events beyond the SM expectation is observed. Upper limits are determined for the production cross section of the new-physics processes mentioned in Section ???. For each model, a 95% confidence level (CL) upper limit is obtained utilizing the asymptotic criterion [?, ?, ?], using a test statistic based on the negative logarithm of the likelihood in Section 3.7.

Figure 3-18 shows the 95% CL upper cross section limits with respect to the corresponding theoretical cross section ( $\mu_{95} = \sigma_{95\%}/\sigma_{\text{theory}}$ ) for the vector and axial-vector mediator scenarios, in the  $M_{\text{med}} - m_{\text{DM}}$  plane. The solid black (dashed red) curves are the observed (expected) contours of  $\mu_{95} = 1$ . The  $\sigma_{\text{theory}}$  hypothesis is

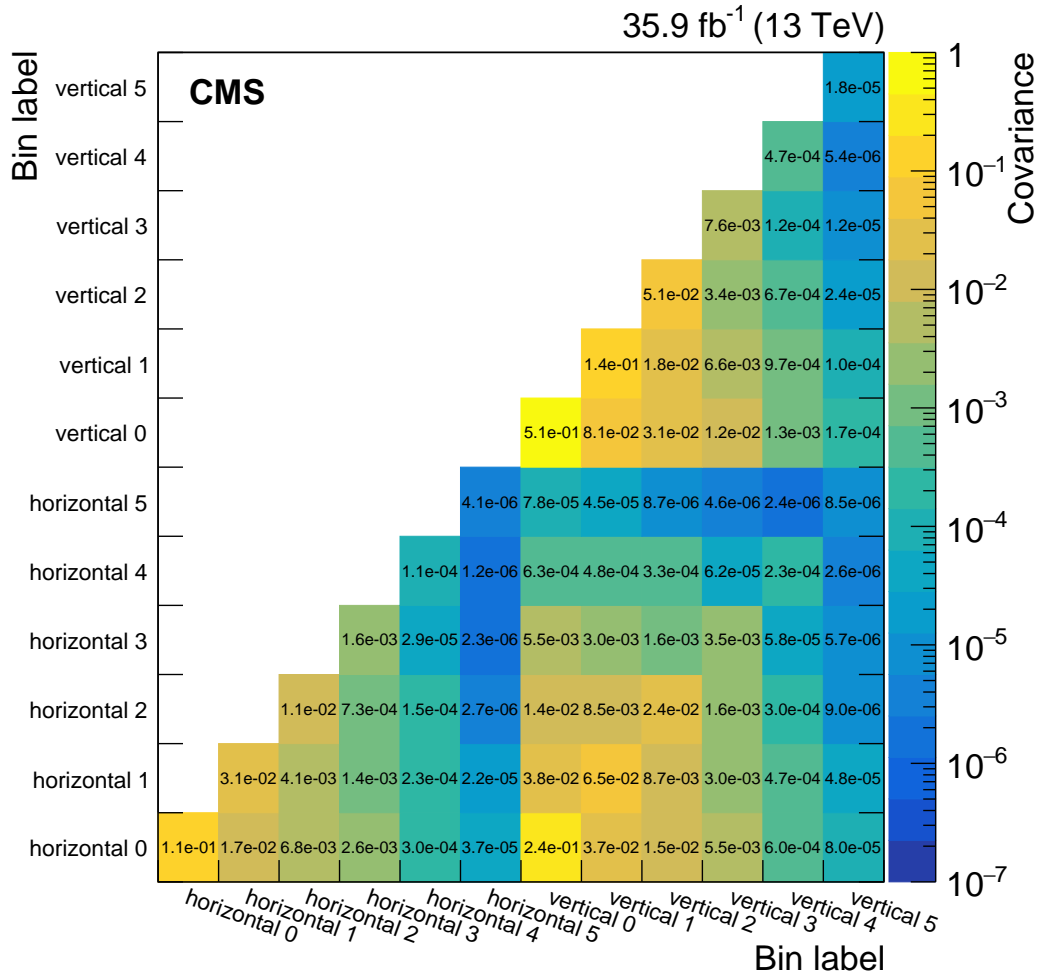


Figure 3-17: Covariances between the predicted background yields in all the  $E_T^\gamma$  bins of the horizontal and vertical signal regions. The bin labels specify which signal region the bin belongs to and what number bin it is for that region.

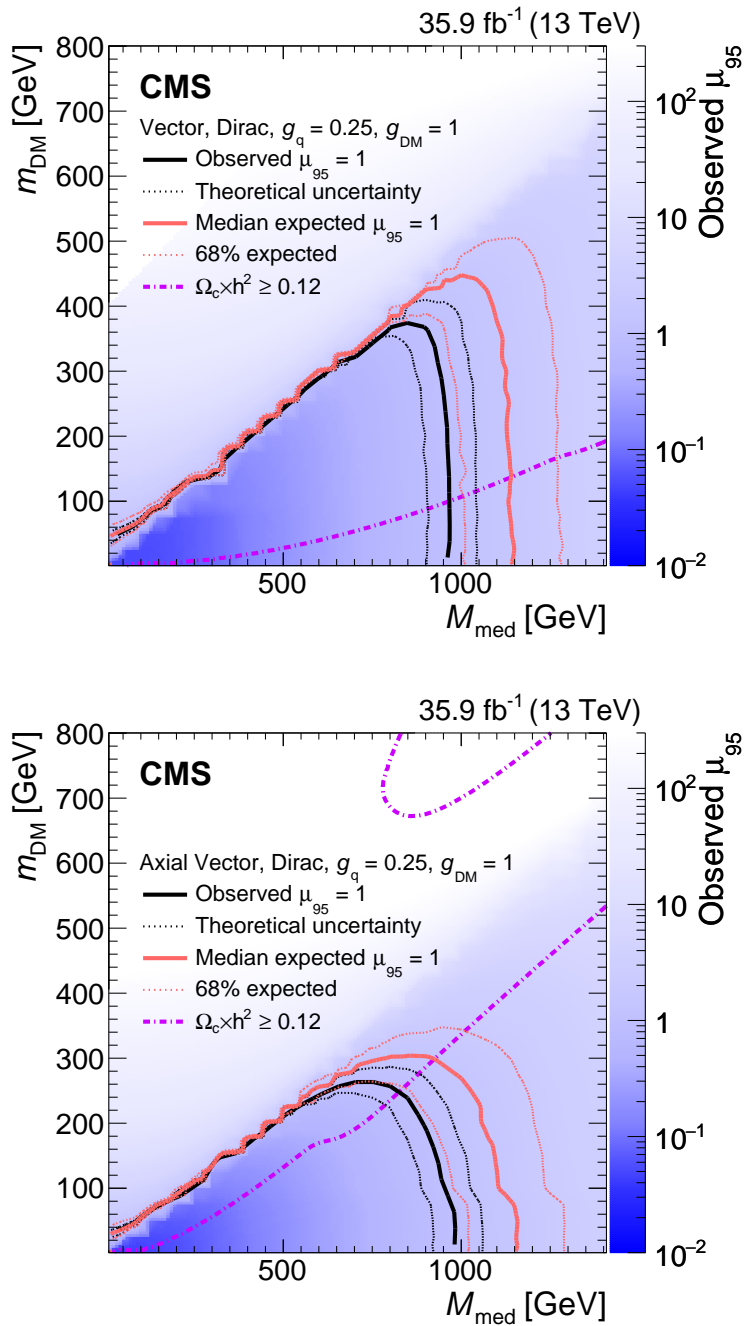


Figure 3-18: The ratio of 95% CL upper cross section limits to the theoretical cross section ( $\mu_{95}$ ), for DM simplified models with vector (top) and axial-vector (bottom) mediators, assuming  $g_q = 0.25$  and  $g_{\text{DM}} = 1$ . Expected  $\mu_{95} = 1$  contours are overlaid in red. The region under the observed contour is excluded. For DM simplified model parameters in the region below the lower violet dot-dash contour, and also above the corresponding upper contour in the right hand plot, cosmological DM abundance exceeds the density observed by the Planck satellite experiment.

excluded at 95% CL or above in the region with  $\mu_{95} < 1$ . The uncertainty in the expected upper limit includes the experimental uncertainties. For the simplified DM LO models considered, mediator masses up to 950 GeV are excluded for values of  $m_{\text{DM}}$  less than 1 GeV.

The results for vector and axial-vector mediators are compared to constraints from the observed cosmological relic density of DM as determined from measurements of the cosmic microwave background by the Planck satellite experiment [?]. The expected DM abundance is estimated, separately for each model, using the thermal freeze-out mechanism implemented in the MADDM [?] framework and compared to the observed cold DM density  $\Omega_c h^2 = 0.12$  [?], where  $\Omega_c$  is the DM relic abundance and  $h$  is the dimensionless Hubble constant.

To enable a direct comparison with results from direct and indirect detection experiments, the 95% CL limits on the mediator mass for the vector and axial-vector models are translated to 90% CL limits on the spin-independent and spin-dependent DM–nucleon scattering cross sections,  $\sigma_{\text{SI}}$  and  $\sigma_{\text{SD}}$  respectively, following the prescriptions given in Ref. [?] and [?]. The exclusion contours for the vector and axial-vector models shown in Figure 3-18 are translated into the  $\sigma_{\text{SI}} - m_{\text{DM}}$  and  $\sigma_{\text{SD}} - m_{\text{DM}}$  planes shown in Figure 3-19. When compared to recent results by the CDMSLite [?], LUX [?], PandaX-II [?], XENON1T [?], and CRESST-II [?] collaborations, the limits obtained from this search provide stronger constraints for DM masses less than 2 GeV for spin independent models. When compared to recent results by the PICO-60 [?], IceCube [?], PICASSO [?] and Super-Kamiokande [?] collaborations, the limits obtained from this search provide stronger constraints for DM masses less than 200 GeV for spin dependent models.

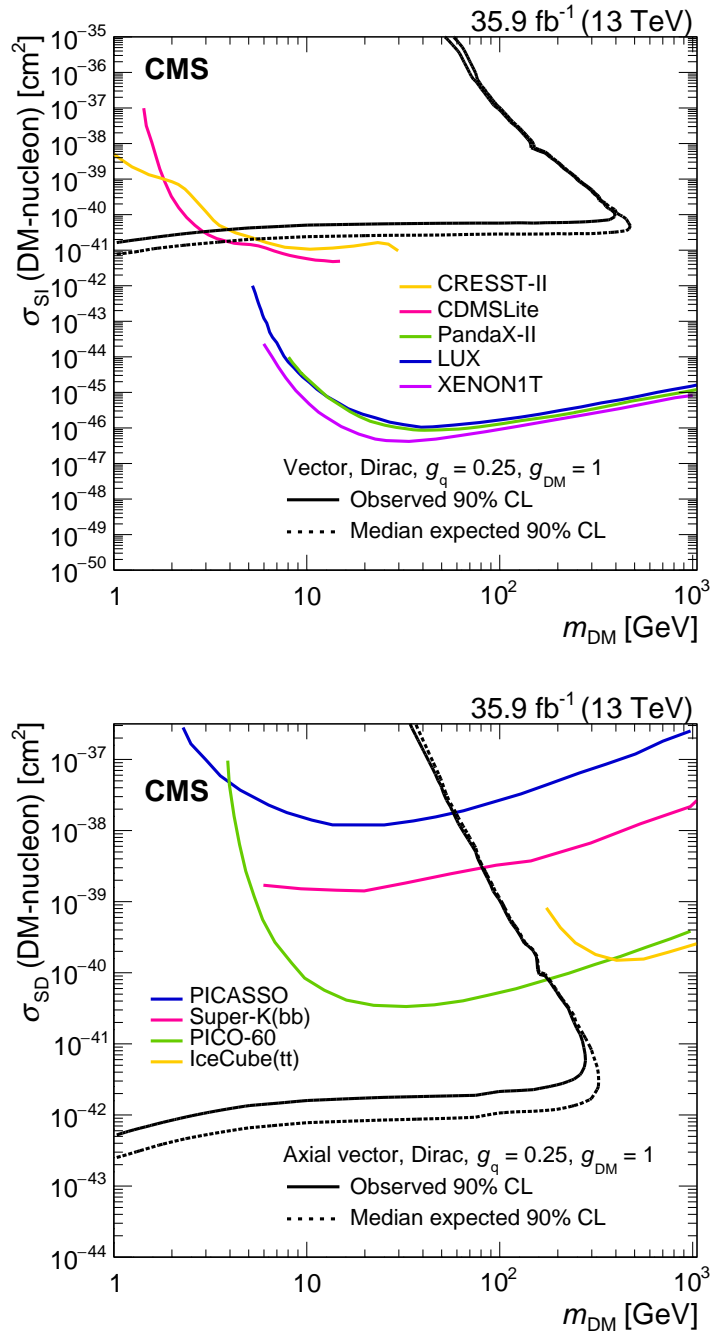


Figure 3-19: The 90% CL exclusion limits on the  $\chi$ -nucleon spin-independent scattering cross sections involving the vector operator (top) and the  $\chi$ -nucleon spin-dependent scattering cross sections involving the axial-vector operator (bottom) as a function of the  $m_{\text{DM}}$ . Simplified model DM parameters of  $g_q = 0.25$  and  $g_{\text{DM}} = 1$  are assumed. The region to the upper left of the contour is excluded. On the plots, the median expected 90% CL curve overlaps the observed 90% CL curve. Also shown are corresponding exclusion contours, where regions above the curves are excluded, from the recent results by the direct and indirect detection experiments listed in the text..